CMS Physics Analysis Summary

Contact: cms-pog-conveners-jetmet@cern.ch 2010/07/21

Jet Performance in pp Collisions at $\sqrt{s}$=7 TeV

The CMS Collaboration

Abstract

We present the techniques adopted by CMS to measure the jet energy response and resolutions. Results from detailed Monte Carlo studies are compared with preliminary observations from the collider data based on up to 73 nb^{-1} of proton-proton LHC collisions at 7 TeV center of mass energy. Studies for jet energy response and resolutions are presented for three different approaches to reconstruct jets in the CMS detector: calorimeter-only based jet reconstruction; the "Jet-Plus-Track" algorithm, which improves the measurement of calorimeter jets by exploiting the associated tracks; and the "Particle Flow" method, which aims to reconstruct each particle in the event based on information from all sub-detectors, prior to the jet clustering. Current physics analyses in CMS use 10% (5%) jet calibration uncertainties for calorimeter jets (Jet-Plus-Track and Particle Flow jets), with the additional 2% uncertainty per unit rapidity. Observations from the current limited statistics datasets support these numbers as conservative estimates. The 10% uncertainties are used for evaluation of the systematic errors due to the jet resolutions effects for all three jet types. Observations from the data support this number as a reasonable estimate.

1 Introduction

Jets are experimental signatures of quarks and gluons, which are produced in high energy processes such as the hard scattering of partons in pp collisions. Due to their large production cross section, jets at LHC will facilitate early studies of new kinematic regimes, confronting predictions of perturbative QCD and probing physics processes within and beyond the standard model. A detailed understanding of the energy calibration and resolution of jets is of crucial importance and is a leading source of systematic uncertainty for many analyses with jets in the final state.

In this paper we discuss the response and resolution performance of various types of jets. We compare Monte Carlo (MC) expectations with results from the collision data, thus helping to validate the MC simulation and to commission the physics program of the CMS experiment [1].

Section 2 describes the different types of jet reconstruction employed by CMS and studied here. Datasets used and the jet quality criteria applied are described in Section 3. Studies of jet energy calibration are discussed in Section 4. Section 5 describes jet p_{T} and position resolution studies. Section 6 discusses jet energy scale and resolution uncertainties. Section 7 summarizes the results.

2 Jet reconstruction at CMS

Four types of jets are reconstructed at CMS, which differently combine individual contributions from subdetectors to form the inputs to the jet clustering algorithm: calorimeter jets, Jet-Plus-Track (JPT) jets, Particle-Flow (PFlow or PF) jets, and track jets. Here we concentrate on the former three types, but also discuss track jets in the context of the jet position resolution studies. Jets in the studies presented here are reconstructed using the Anti-k_{T} [2] clustering algorithm with the size parameter $R = 0.5$. To evaluate their performance, in Monte Carlo simulations "generator jets" (GenJets) or "particle jets" are reconstructed as well by applying the same jet clustering algorithm to all stable generated particles ("MC truth"). These generator jets are then associated to jets reconstructed from the simulated detector signals, by requiring a small distance $\Delta R = \sqrt{\Delta\eta^2 + \Delta\phi^2}$ between the jet axes in $\eta - \phi$ space.

Calorimeter jets are reconstructed using energy deposits in the electromagnetic (ECAL) and hadronic (HCAL) calorimeter cells, combined into calorimeter towers. A calorimeter tower consists of one or more HCAL cells and the geometrically corresponding ECAL crystals. In the barrel region of the calorimeters ($|\eta| < 1.4$), the unweighted sum of one single HCAL cell and 5x5 ECAL crystals form a projective calorimeter tower. The association between HCAL cells and ECAL crystals is more complex in the endcap regions of the electromagnetic calorimeter ($1.4 < |\eta| < 3.0$). In order to suppress the contribution from calorimeter readout electronics noise, thresholds are applied on energies of individual cells when building towers for reconstruction of jets and missing transverse energy (E_T^{miss}). These thresholds are listed in Table 1. In addition, to suppress contribution from event pile-up (additional proton-proton interactions in the same bunch crossing), calorimeter towers with transverse energy of $E_T^{towers} < 0.3$ GeV are not used in jet reconstruction.

The **Jet-Plus-Tracks** algorithm [3] exploits the excellent performance of the CMS tracking detectors to improve the p_{T} response and resolution of calorimeter jets. Calorimeter jets are reconstructed first as described above, then charged particle tracks are associated with each jet based on spatial separation in $\eta - \phi$ between the jet axis and the track momentum measured at the interaction vertex. The associated tracks are projected onto the surface of the calorimeter

Section	Threshold (in GeV)
HB	0.7
HE	0.8
HO	1.1/3.5 (Ring 0/Ring 1,2)
HF (Long)	0.5
HF (Short)	0.85
EB	0.07 (per crystal, double sided)
EE	0.3 (per crystal, double sided)
EB Sum	0.2
EE Sum	0.45

Table 1: Calorimeter offline cell thresholds used in calorimeter and JPT jet reconstruction. The "Section" label refers to the calorimeter subsystems [1]: Hadronic Barrel (HB), Endcap (HE), Outer (HO) and Forward (HF), and ECAL Barrel (EB) and Endcap (EE). Independent thresholds are placed in different sections (rings) of HO, and in different (long and short fiber) readouts in HF. In ECAL, in addition to energy thresholds on readouts from individual crystals, thresholds are applied on the sum of crystal readouts corresponding to the same tower.

and classified as in-cone tracks if they point to within the jet cone around the jet axis on the calorimeter surface. If the 3.8 T magnetic field of CMS has instead bent the track out of the jet cone, it is classified as a out-of-cone track. The momenta of both in-cone and out-cone tracks are then added to the energy of the associated calorimeter jet. For in-cone tracks the expected average energy deposition in the calorimeters is subtracted based on the momentum of the track. The direction of the axis of the original calorimeter jet is also corrected by the algorithm.

The **Particle Flow** algorithm combines the information from all CMS sub-detectors to identify and reconstruct all particles in the event, namely muons, electrons, photons, charged hadrons and neutral hadrons. The detailed description of the algorithm and its commissioning can be found in References [4, 5]. Charged hadrons, in particular, are reconstructed from tracks in the central tracker. Photons and neutral hadrons are reconstructed from energy clusters in the electromagnetic and hadron calorimeters. Clusters separated from the extrapolated position of tracks in the calorimeters constitute a clear signature of these neutral particles. A neutral particle overlapping with charged particles in the calorimeters can be detected as a calorimeter energy excess with respect to the sum of the associated track momenta. PFlow jets are then reconstructed from the resulting list of particles. The jet momentum and spatial resolutions are expected to be improved with respect to calorimeter jets as the use of the tracking detectors and of the excellent granularity of the ECAL allows to resolve and precisely measure charged hadrons and photons inside jets, which constitute $\sim$90% of the jet energy.

Track jets [6] are reconstructed from tracks of charged particles measured in the central tracker. Only well measured tracks, based on their association with the primary vertex and their quality, are used by the algorithm. The method is completly independent from the calorimetric measurements, allowing for cross-checks. Detailed description of the track jet performance is given in Reference [6].

3 Data and jet selection

Data used for the studies presented here were recorded by the CMS detector during March - July 2010 in proton-proton collisions at LHC at $\sqrt{s} = 7$ TeV and correspond to the integrated luminosity of up to $L_{int} = 73\,\text{nb}^{-1}$. In various studies we use Zero Bias, Minimum Bias, dijet p_{T} average, single photon, and single jet triggers which are described in later sections. In all cases,

a veto on triggers which indicate the occurrence of beam halo effects are applied. The events are further filtered based on their signature in the pixel detector: the fraction of high-purity tracks [7] with respect to the total number of tracks was required to be at least 20 % for events with at least ten tracks.

CMS has developed jet quality criteria ("Jet ID") for calorimeter jets [8] and PFlow jets which are found to retain the vast majority of real jets in the simulation while rejecting most fake jets arising from calorimeter and/or readout electronics noise. These are studied in pure noise non-collision data samples such as cosmic trigger data or data from triggers on empty bunches during LHC operation. To pass Jet ID, calorimeter jets are required to have electromagnetic energy fraction EMF>0.01 if within the ECAL fiducial region of $|\eta| < 2.6$; the number of calorimeter cells containing 90% of jet energy must be $n^{90}_{\text{hits}} > 1$; and the fraction of jet energy in the hottest Hybrid Photo Detector (HPD) unit of the HCAL readout within the jet must be $f_{\text{HPD}} < 0.98$. Detailed explanations of n^{90}_{hits} and f_{HPD} are given in Ref. [8]. JPT jets are treated as calorimeter jets with respect to the quality criteria. The PFlow jets are required to have charged hadron fraction $CHF > 0.0$ if within tracking fiducial region of $|\eta| < 2.4$, neutral hadron fraction $NHF < 1.0$, charged electromagnetic (electron) fraction $CEF < 1.0$, and neutral electromagnetic (photon) fraction $NEF < 1.0$. These requirements remove fake jets arising from spurious energy depositions in a single sub-detector. Jets in the presented studies are required to pass Jet ID criteria.

4 Jet Energy Calibration

Jet energy measured in the detector is typically different from the corresponding particle jet energy. The latter is obtained in the simulation by clustering, with the same jet algorithm, the stable particles produced during the hadronization process that follows the hard interaction. The main cause for this energy mismatch is the non-uniform and non-linear response of the CMS calorimeters. Furthermore, electronics noise and additional pp interactions in the same bunch crossing (event pile-up) can lead to extra unwanted energy. The purpose of the jet energy correction is to relate, on average, the energy measured in the detector to the energy of the corresponding particle jet.

CMS has developed a factorized multi-step procedure for the jet energy calibration (JEC) [9]. The following three subsequent (sub-)corrections are devised to correct calorimeter, PFlow and JPT jets to the corresponding particle jet level: offset, relative and absolute corrections. The offset correction aims to correct the jet energy for the excess unwanted energy due to electronics noise and pile-up. The relative correction removes variations in jet response versus jet η relative to a central control region chosen as a reference because of the uniformity of the detector. The absolute correction removes variations in jet response versus jet p_{T}. The default sequence for the jet energy corrections is expressed mathematically as:

$$E_{Corrected} = (E_{Uncorrected} - E_{offset}) \times C_{Rel}(\eta, p''_{\text{T}}) \times C_{Abs}(p'_{\text{T}}) \quad (1)$$

where p''_{T} is the transverse momentum of the jet corrected for offset and $p'_{\text{T}} = p''_{\text{T}} \times C_{Rel}(\eta, p''_{\text{T}})$ is the transverse momentum of the jet corrected for offset and pseudorapidity dependence.

CMS pursues two complementary approaches to determine the jet energy correction factors: utilizing MC truth information (MC truth JEC), and using physics processes from pp collisions for in-situ jet calibration. At the current initial stage of LHC running, MC truth JEC is used to correct jets in both data and MC simulation. At the same time, we have carried out in-

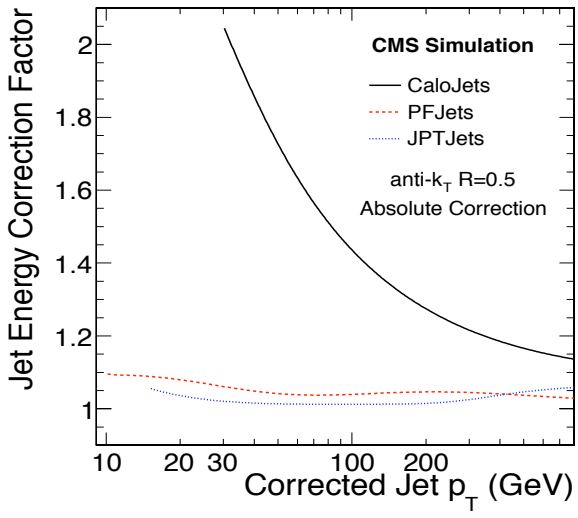

Figure 1: Absolute jet energy correction factors C_{Abs} derived from simulation for calorimeter, JPT, and PFlow jets at $\sqrt{s} = 7$ TeV as a function of corrected jet transverse momentum.

situ calibration studies using various physics processes from LHC data. These measurements, while currently statistically limited, provide initial confirmation for the MC truth JEC. As the size of the calibration samples increases with increasing LHC luminosity, in-situ calibration constants will replace those extracted from the MC truth.

In the following two sub-sections we describe the MC truth and the in-situ jet calibration studies.

4.1 Monte Carlo truth jet energy correction

Monte Carlo truth jet energy corrections are derived using PYTHIA [10] QCD events at $\sqrt{s}$= 7 TeV proton-proton collisions which are further processed through a full CMS GEANT4 [11] simulation of the CMS detector. In these events, we reconstruct calorimeter, JPT, and PFlow jets, as well as particle jets from the four-momenta of the MC particles (in the following referred to as GenJets). GenJets are matched to the calorimeter jets (or JPT / PFlow jets) in η-ϕ space by requiring ΔR <0.25. For the matched jets, we study the quantity p_T^{Jet}/p_T^{GenJet} to extract jet calibration factors as a function of uncalibrated jet p_{T} and η.

The MC-truth jet energy corrections as described below do not factorize out the offset correction. Rather, the offset is lumped together with the relative and absolute corrections. (Detailed discussion about the size of the offset in the current LHC data and in MC is given in the next section.) Following this approach, the extraction procedure has two steps: first we extract the relative correction $C_{Rel}(\eta, p_{\mathrm{T}})$ by comparing the response at a given η to that of jets in the central region $|\eta|$ <1.3. In the second step, we extract the absolute correction $C_{Abs}(p'_{\mathrm{T}})$ that removes the p_{T} dependence of the jet response, and brings it to unity. Figure 1 shows absolute correction factors C_{Abs} as a function of corrected jet transverse momentum for the three jets types. At low transverse momentum, calorimeter jets need to be corrected by a large multiplicative factor (up to 2) due to non-compensating nature of the CMS calorimeters. JPT and PFlow jets require much smaller corrections as these jets rely heavily on the tracking information.

The combined correction factor $C(p_{\mathrm{T}}, \eta)$ multiplies each component of the jet momentum four-vector P_μ (components indexed by μ in the following):

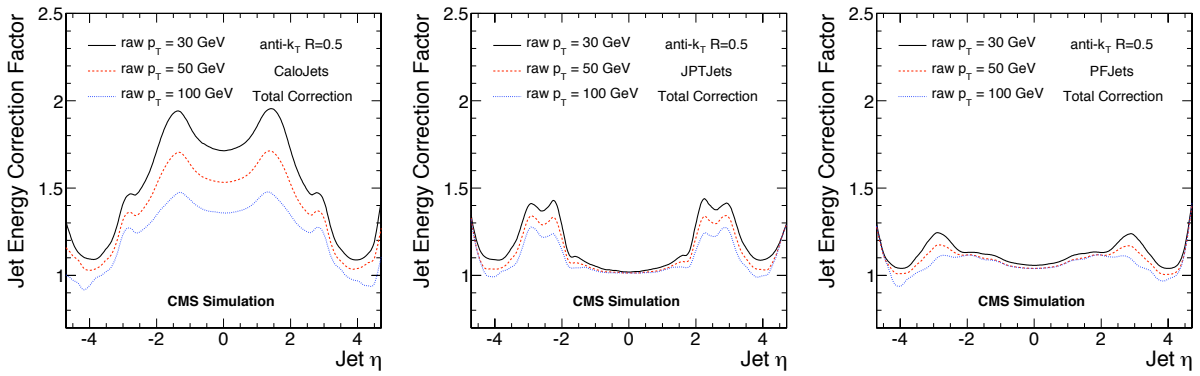

Figure 2: Total jet energy correction factors $C(p_{\mathrm{T}}, \eta)$ derived from simulation for calorimeter (left), JPT (center), and PFlow (right) jets at $\sqrt{s} = 7$ TeV as a function of jet η for three different values of raw (uncorrected) jet p_{T}.

$$P_{\mu}^{cor} = C(p_{\mathrm{T}}, \eta) \times P_{\mu} \tag{2}$$

where

$$C(p_{\mathrm{T}}, \eta) = C_{Rel}(\eta, p_{\mathrm{T}}) \times C_{Abs}\left(p_{\mathrm{T}} \times C_{Rel}(\eta, p_{\mathrm{T}})\right) \tag{3}$$

Figure 2 shows the MC-truth jet energy correction factors $C(p_{\mathrm{T}}, \eta)$ for calorimeter, JPT and PFlow jets. The factors are shown as a function of η at three representative values of jet p_{T}. There is a clear structure in the pseudorapidity dependence of $C(p_{\mathrm{T}}, \eta)$, most pronounced for the calorimeter jets, which naturally divides the detector in three calorimeter regions: barrel ($|\eta|$ <1.3), endcaps ($1.3 < |\eta| < 3$) an forward ($3 < |\eta| < 5$). Correction factors at higher $|\eta|$ are smaller for calorimeter jets, because a fixed p_{T} corresponds to a larger energy at higher $|\eta|$, and hence to a larger (smaller) energy response (correction factor). As expected, overall correction factors are smaller for JPT and PFlow jets, particularly in $|\eta|$ regions where these jet types employ tracking information ($|\eta| < 2.0$ for the JPT jets and $|\eta| < 2.5$ for the PFlow jets).

To test the accuracy of the MC truth corrections, we perform a validation test by re-deriving $C(p_{\mathrm{T}}, \eta)$ for the JEC-corrected jets. As expected, we observe a total correction factor consistent with unity well within 2%. Small variations within this value are due to available MC statistics and the fit residuals. We assign 2% uncertainty on MC truth JEC for jets in simulation. The JEC uncertainties for jets in the collider data are inferred from in-situ calibration studies and are discussed in the following sections.

4.2 In-situ jet energy calibration

4.2.1 Offset correction

The offset correction is the first step in the chain of the factorized corrections. Its purpose is to estimate and subtract the energy not associated with the high-p_{T} scattering. The excess energy includes contributions from calorimeter electronic noise and extra pp interactions within the same bunch crossing (pile-up). The feasibility study of the offset for CMS is described in [12].

The number of additional inelastic pp interactions that produce event pile-up follows a Poisson distribution with average given by $< N_{PU} >= \sigma_{\mathrm{inel}} \mathcal{L}_{\mathrm{bunch}}$, where $\sigma_{\mathrm{inel}} = 71$ mb [10] is the total inelastic pp cross section at $\sqrt{s} = 7$ TeV, and $\mathcal{L}_{\mathrm{bunch}}$ is the integrated luminosity of the two colliding bunches. For the data-taking period of March 30 – July 4, the average number of pile-up ranges from $< N_{PU} > \simeq 0.001$ for early runs up to $< N_{PU} > \simeq 0.5$.

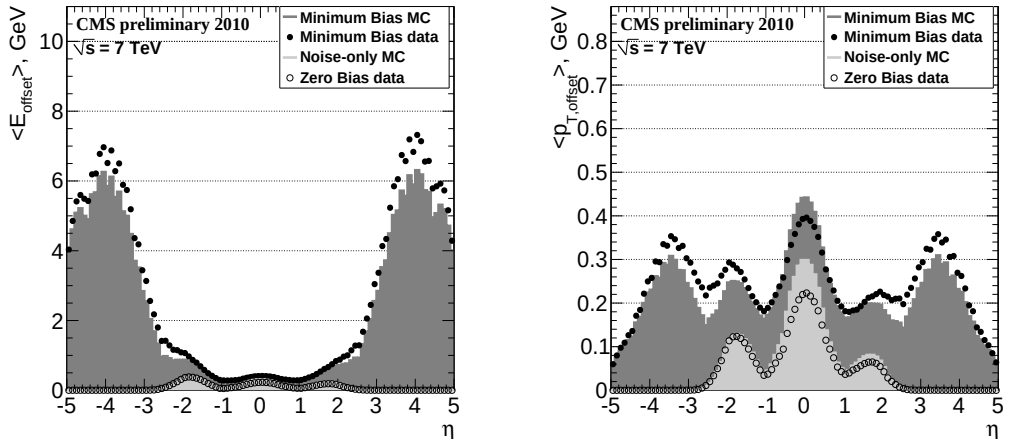

Figure 3: Offset contributions from noise-only and from noise+one pile-up: energy (left) and p_{T} (right) as a function of η.

We separately measure offset components arising from noise, noise + one pile-up, as well as the total average (over the considered dataset) offset.

To estimate the noise-only contribution, we use events from random trigger, without any preconditions except a beam crossing, referred to as Zero Bias trigger. In these events, we veto the Minimum Bias trigger events. The latter require coincidence hits in the Beam Scintillating Counters [1], which indicate pp interaction taking place in the given bunch crossing. Vetoing the Minimum Bias trigger events gives us a pure noise sample. In this sample, we study the variable $E_{\mathrm{offset}}(\eta)$ which is the average calorimeter energy summed up inside a cone of radius $R_{\mathrm{cone}} = 0.5$ at a given η.

To estimate the offset from one additional interaction event, we select Minimum Bias trigger events in early runs, (where the fraction of events with more than one interaction per bunch crossing is small) and study $E_{\mathrm{offset}}(\eta)$. The measured energy then can be attributed to noise+one pile-up.

Figure 3 shows the offset $E_{\mathrm{offset}}(\eta)$ for noise and noise+one pile-up. It also shows the offset in $p_{T\,offset}(\eta)$. The contribution from noise is less than 250 MeV in p_{T} over the entire η range.

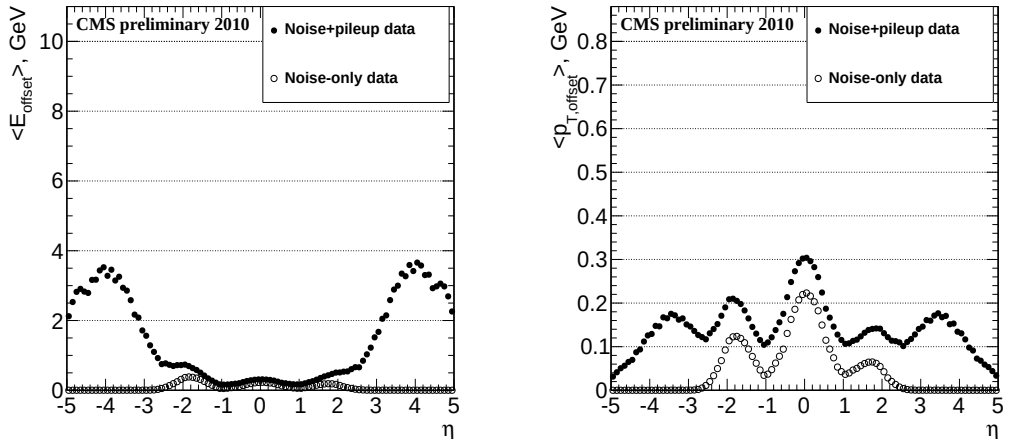

Figure 4: Total average offset (markers): energy (left) and p_{T} (right) as a function of η. Contribution from noise-only is also shown.

Contribution from noise + one pile-up is ∼450 MeV in energy in the central region. In forward region, the contribution increases up to 7 GeV in energy, but still remains relatively small in p_T, up to 400 MeV. The figure also shows expectation from the MC simulation. We use PYTHIA Minimum Bias sample for pile-up, and single neutrino MC events for noise-only sample. The agreement between data and MC is reasonable for both, noise and pile-up.

Finally, the total average offset (over March 30 – July 4 dataset) is determined from inclusive Zero Bias events (with no veto on Minimum Bias triggers), which naturally has contributions from both noise and pile-up, and is representative of the energy offset underneath a jet in an event collected with a high-p_T trigger at the same luminosity and running conditions. The total average offset is shown in Figure 4. As can be seen, it has large contribution from noise in $|\eta| < 2.5$ region, with pile-up contribution becoming dominant beyond $|\eta| = 2.5$.

Given that we see relatively modest contributions from both, noise and pile-up, and the fact that on average 50% of high-p_T events have additional pile-up overlaid, which translates into small average total offset as shown in Figure 4, we do not currently correct jets for the offset correction. However, the estimate of the offset as obtained from Zero Bias and Minimum Bias events can be substantially smaller than the true offset energy because Zero Suppression has a different impact on noise and extra energy that lands inside a jet than it does when it lands in the low occupancy environment typical of Zero Bias and Minimum Bias events. In regions where noise, pile-up and jet contributions overlap, contributions from noise and pile-up are added on top of the real jet energy, making it easier for these unwanted contributions, as well as for the real jet energy, to pass above the Zero Suppression thresholds. As a result, the real offset underneath a jet is expected to be higher than the offset estimated from the Zero Bias / Minimum Bias data events. Earlier studies [12] indicate that difference between the estimated and the true offset can be as large as factor 4. In that case not correcting for the offset introduces systematic error of 2% for the calorimeter jets with $p_T = 50$ GeV in those events where we have one pile-up overlay. Since offset energy is a linear function of the number of additional pile-up overlay [12], the systematic uncertainty also increases linearly with $< N_{PU} >$. The overall systematic effect for the current data sample where we have 50% of events with pile-up overlay, is small, at the level of 1% at $p_T = 50$ GeV, and decreases linearly with p_T. The small discrepancy in the noise-only offset between data and MC also introduces additional systematics which amounts to 2% for calorimeter jets at $p_T = 20$ GeV, and decreases gradually for the higher p_T's.

4.2.2 Relative response from dijet p_T balance

To derive the relative energy corrections from collider data, we employ the dijet p_T balance technique, first used at SPPS [13], and later refined by the Tevatron experiments [14, 15]. Detailed description of the feasibility study of the method for CMS is given in Reference [16]. The idea is to use p_T balance in back-to-back dijet events with one jet (barrel jet) in the central control region of the calorimeter, $|\eta| < 1.3$, and the other jet (probe jet) at arbitrary η. The central region is chosen as reference because of the uniformity of the detector [1], and because it has highest jet transverse momentum reach.

To collect an unbiased dijet calibration sample, CMS has devised dedicated High Level Triggers which fire on the average uncorrected $p_T = (p_{T1} + p_{T2})/2$ of the two leading jets above thresholds of 15 GeV and 30 GeV. The dataset from dijet p_T average trigger with the 15 GeV threshold, which is prescaled, corresponds to $L_{int} = 20$ nb^{-1} integrated luminosity. Unprescaled dijet p_T average trigger with the 30 GeV threshold gives us $L_{int} = 71$ nb^{-1} luminosity.

Offline, events are required to contain at least two jets, with one of them in the barrel region

of $|\eta|$ <1.3. To enrich the sample in $2 \to 2$ process, the two leading jets must be azimuthally separated by $\Delta\phi > 2.7$ rad. Furthermore, no additional jets with $p_{\mathrm{T}}^{3rdJet} / p_{\mathrm{T}}^{dijet} > 0.2$ are allowed. Here $p_{\mathrm{T}}^{dijet} = (p_{\mathrm{T}}^{probe} + p_{\mathrm{T}}^{barrel})/2$ is the average uncorrected p_{T} of the two leading jets. Further selection requires the reconstruction of one good primary vertex (PV) with $|z(\mathrm{PV})| < 15$ cm and $n_{\mathrm{dof}}(\mathrm{PV}) \geq 5$, which means that at least four tracks are considered in the vertex fit; $z(\mathrm{PV})$ represents the position of the proton-proton collision along the beam-line and $z = 0$ indicates the center of the CMS detector.

In the selected event sample we study the distribution of the balance quantity

$$B = \frac{p_{\mathrm{T}}^{probe} - p_{\mathrm{T}}^{barrel}}{p_{\mathrm{T}}^{dijet}} \tag{4}$$

in bins of η^{probe} and p_{T}^{dijet}. To avoid trigger bias, we only use p_{T}^{dijet} values above 18 GeV, 38 GeV and 40 GeV (31 GeV, 60 GeV and 63 GeV) for calorimeter, JPT and PFlow jets, in data collected by the dijet average trigger with 15 GeV (30 GeV) threshold. This selection of minimal p_{T}^{dijet}, determined from data, guarantees that the efficiency of the dijet average triggers is higher than 99%. Distributions of the balance variable B for the three jet types in various representative p_{T}^{dijet} and η^{probe} bins are shown in Figure 5. Data observations are compared to Monte Carlo expectations extracted from PYTHIA QCD dijet events applying the same procedure.

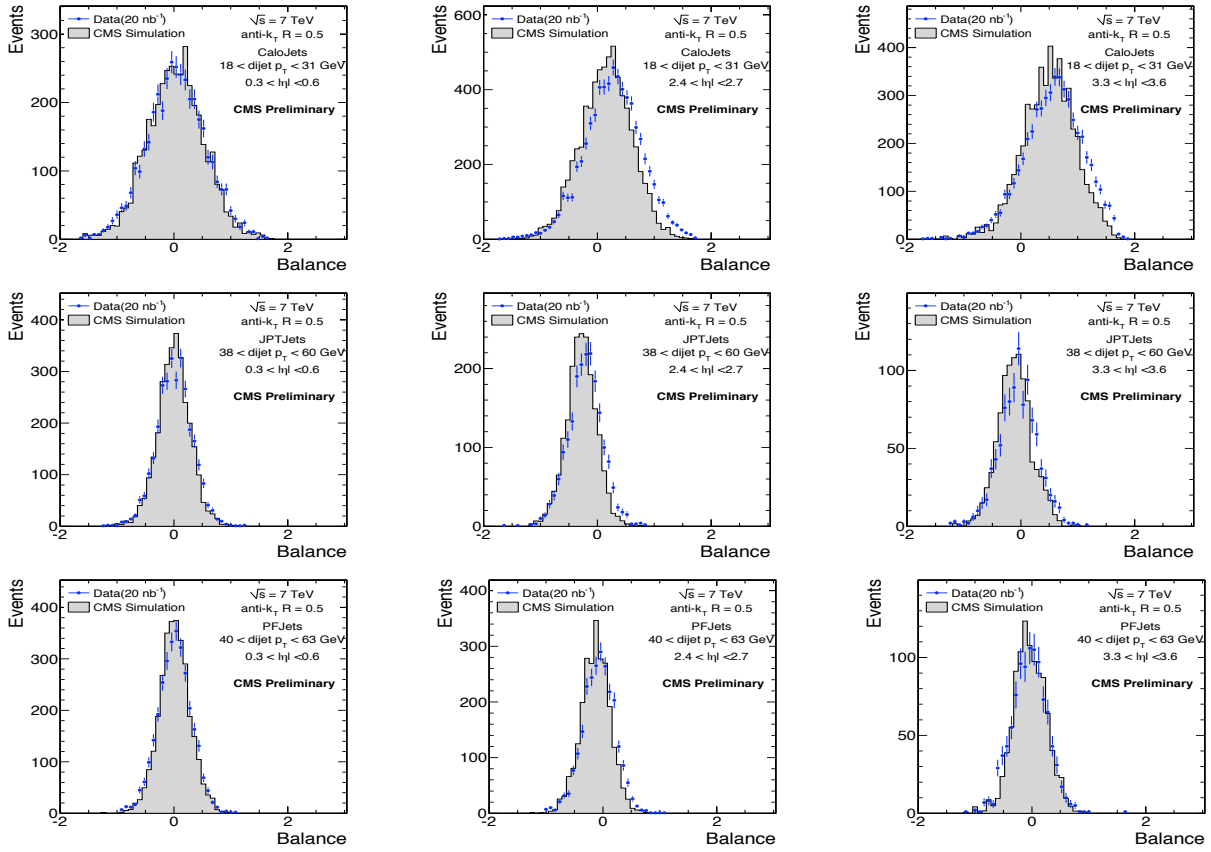

Figure 5: Distribution of balance variable B for calorimeter (top), JPT (middle) and PFlow (bottom) jets in various p_{T}^{dijet}, η^{probe} bins.

The average value of the B distribution, $< B >$, in a given η^{probe} and p_{T}^{dijet} bin is used to determine the relative response

$$R(\eta^{probe}, p_{\mathrm{T}}^{dijet}) = \frac{2+ < B >}{2- < B >} \tag{5}$$

The R variable is the least biased estimator of the relative response (as opposed to e.g. $p_{\mathrm{T}}^{probe} / p_{\mathrm{T}}^{barrel}$ which exhibits a large bias). Figure 6 shows the relative jet response for calorimeter jets, as a function of $|\eta|$ in four different raw p_{T}^{dijet} bins. Measurements of R from positive and negative η bins are consistent within the available statistics, and are therefore combined to double the statistics. The observed variation in $|\eta|$ is biggest at low p_{T}^{dijet} bin, and reflects the transition between barrel and endcap calorimeters at $|\eta|$=1.3, and to a much lesser extent, transition between endcap and forward calorimeters at $|\eta|$=3. Higher relative response at large values of $|\eta|$ is due to higher energies of forward jets compared to the central ones for a given value of p_{T}. Figures 7 and 8 show the relative response for JPT and PFlow jets as a function of $|\eta|$ in four different p_{T}^{dijet} bins. The response variations with $|\eta|$ here are less reflective of calorimeter structure, as these jets rely heavily on the CMS tracker.

Figures 6-8 also show MC expectations obtained by applying the same dijet balance technique

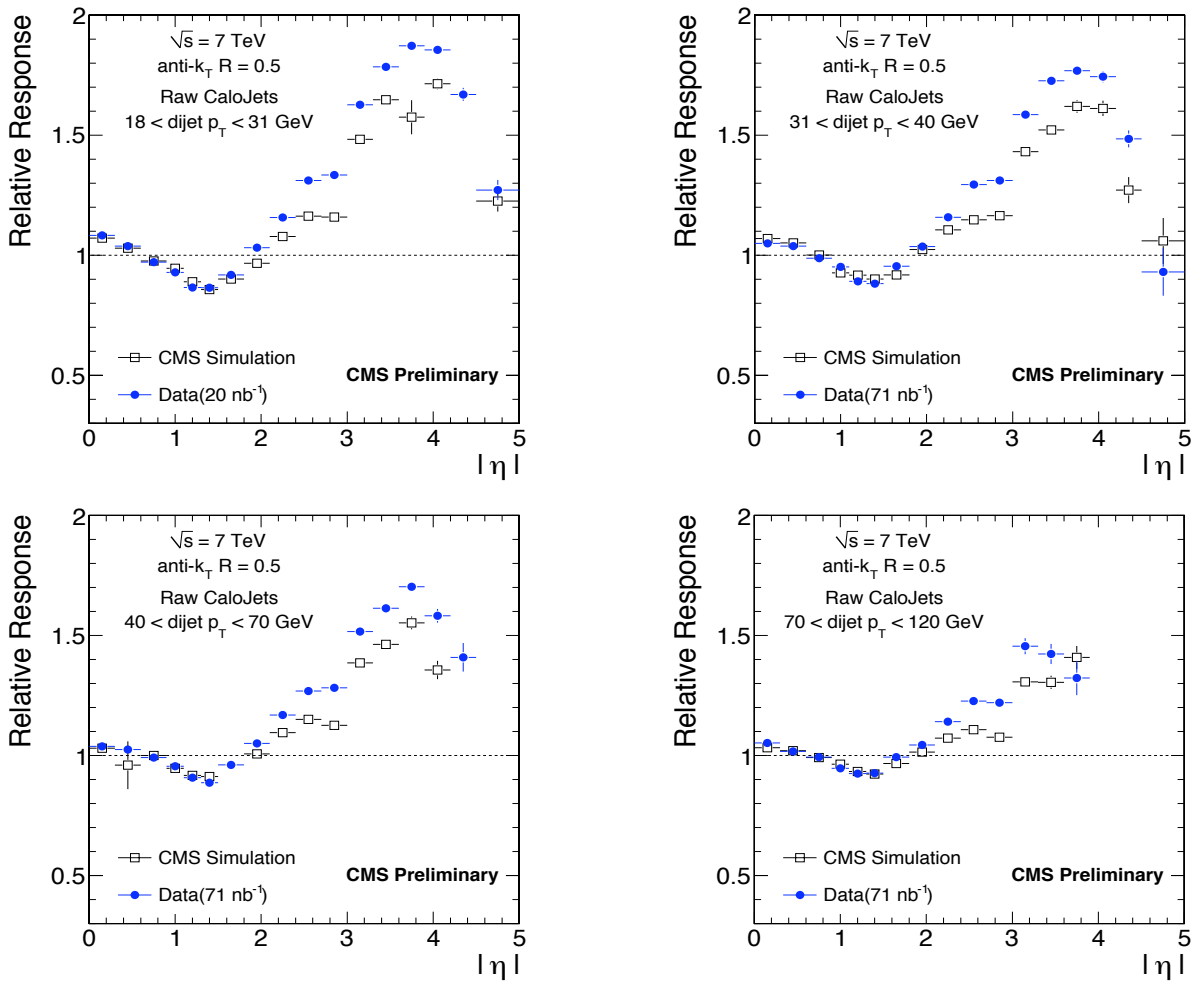

Figure 6: Relative jet energy response for Calorimeter jets in various p_{T}^{dijet} bins.

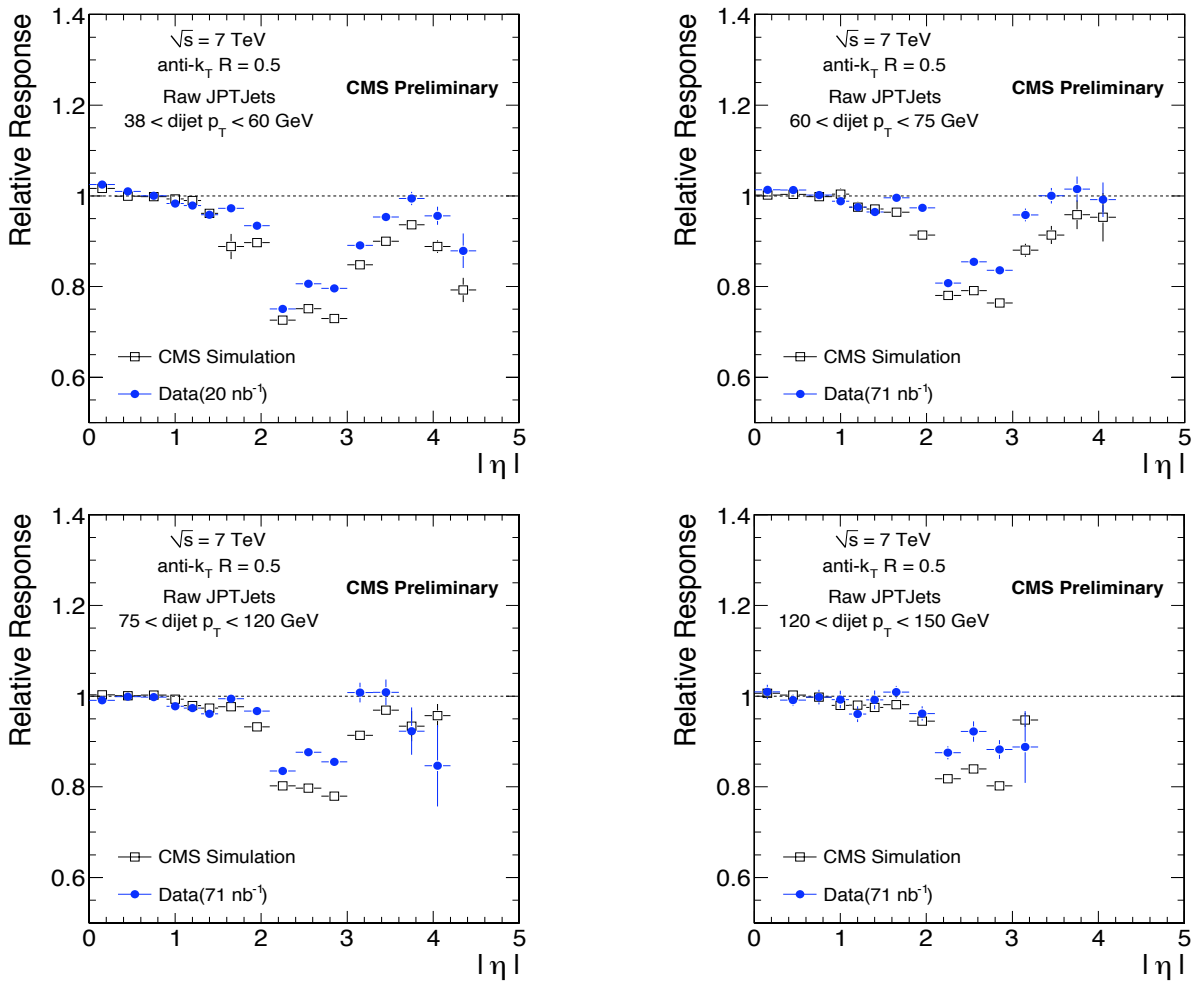

Figure 7: Relative jet energy response for JPT jets in various p_{T}^{dijet} bins.

to the simulated QCD dijet events. As can be seen, data and MC are in good agreement for $|\eta| < 2.0$, whereas in the $|\eta| > 2.0$ region the relative response in data is up to ∼10% higher compared to the simulation. This observation is consistent with results from single particle response studies [17], where the same trend of higher data response is seen in $|\eta| > 2.0$ region. Work is going on to improve calorimeter response simulation in CMS, particularly for this high $|\eta|$ regions.

Figure 9 shows the data/MC ratio for the relative response, as measured with the dijet balance method, for the nominally (MC truth) corrected jets. The overlaid uncertainty band corresponds to $\pm$ 2%$|\eta|$ range that covers the observed systematic trend of higher data response at the forward $|\eta|$ values.

In order to account for the observed shift in the data, we derived an additional residual correction on top of the nominal MC truth corrections. The residual correction is equal to the difference between the relative response in data with respect to the MC, expressed in terms of the jet η. Figure 10 shows the data/MC ratio for the relative response where jets in data are additionally corrected using the residual correction. The data/MC points are now statistically consistent with unity with no systematic shift observed. Figure 10 also displays the $\pm$ 2%$|\eta|$ error band.

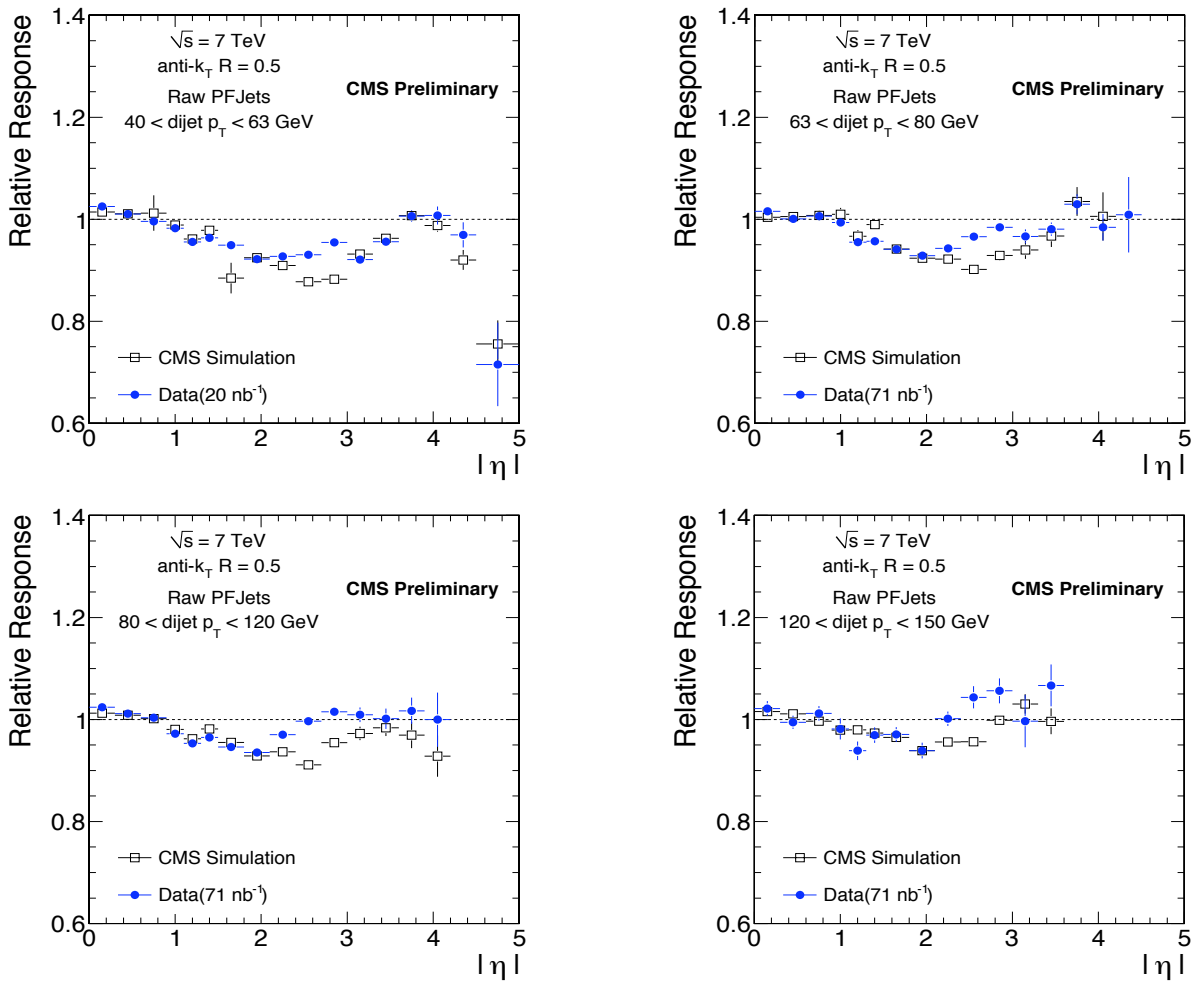

Figure 8: Relative jet energy response for PFlow jets in various p_{T}^{dijet} bins.

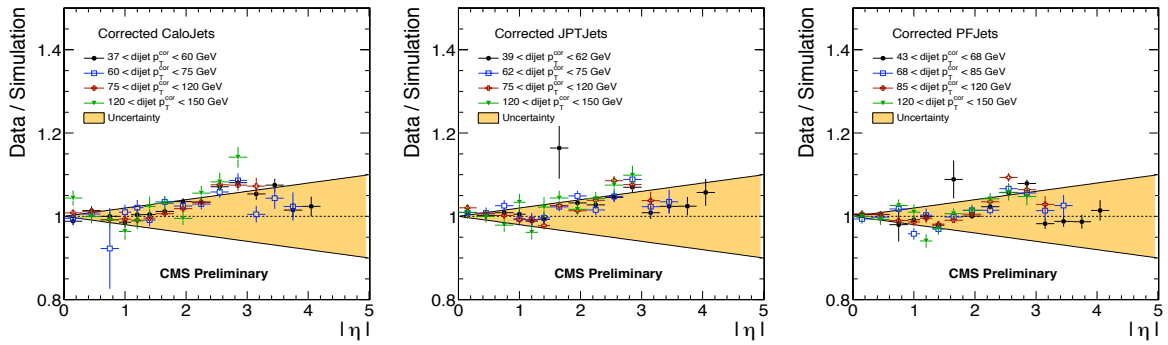

Figure 9: Data/MC ratio for the relative response obtained from the dijet p_{T} balance method for calorimeter (top left), JPT (top right) and PFlow (bottom) jets. The jets in data and MC are corrected for MC-truth JEC. The $\pm$ 2%$|\eta|$ band is overlaid. The few outlying points with large error bars are due to limited statistics in low-p_{T} Monte Carlo samples.

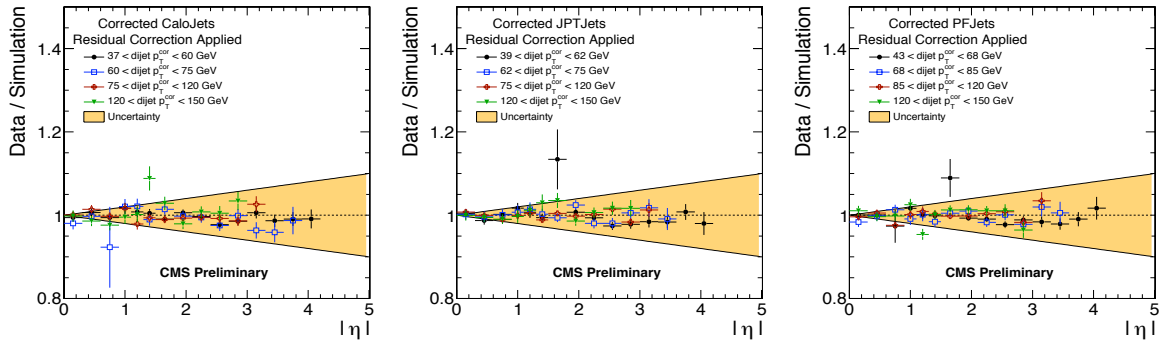

Figure 10: Data/MC ratio for the relative response obtained from the dijet p_{T} balance method for calorimeter (top left), JPT (top right) and PFlow (bottom) jets. The jets in MC are corrected for MC-truth JEC, whereas jets in data are corrected for MC-truth JEC plus the residual correction discussed in the text. The $\pm$ 2%$|\eta|$ band is overlaid. The few outlying points with large error bars are due to limited statistics in low-p_{T} Monte Carlo samples.

Based on these observations, CMS uses $\pm$ 2%$|\eta|$ uncertainty on the relative JEC for physics analyses using either nominal MC-truth JEC or MC-truth JEC supplemented by the residual correction. In the latter case, uncertainty of $\pm$ 2%$|\eta|$ is clearly a conservative estimate, as suggested by Figure 10.

4.2.3 Absolute response measurements from photon+jet events

The CMS calorimeter energy response to a particle level jet is smaller than unity and varies as a function of jet p_{T}. The purpose of the absolute jet energy correction is to remove these variations and make the response equal to unity at all p_{T} values. When combined with the relative correction and the offset correction, the absolute correction provides the complete correction back to the particle jet level required for most CMS analyses.

To determine the absolute jet energy corrections from collider data, we use γ+jet events, and apply two different calibration procedures, called p_{T} balancing and MPF (missing E_T projection fraction) methods, respectively. First we discuss and present results from the p_{T} balancing method which exploits the balance in the transverse plane between the photon and the recoiling jet and uses the photon p_{T}, that is accurately measured in the crystal ECAL calorimeter, as a reference object. The technique was introduced by the Tevatron experiments [14, 15]. The detailed feasibility study of the method for CMS is described in Reference [18].

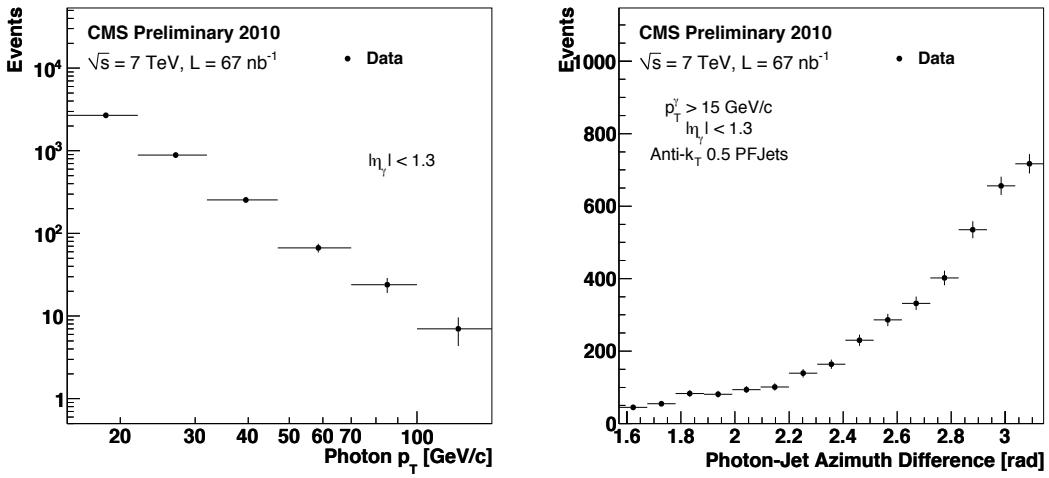

Figure 11: Distribution of photon transverse momentum (left) and azimuthal angle between photon and calorimeter jet (right).

To collect the γ+jet calibration sample, we use High Level single photon triggers above 10 GeV and 15 GeV thresholds. The analyzed data corresponds to an integrated luminosity of $L_{int} = 67$ nb^{-1}. Offline, we require a photon candidate with $p_{\mathrm{T}}^{\gamma} > 15$ GeV within the barrel region of ECAL, $|\eta|$ <1.3. This sample is dominated by overwhelming QCD dijet background, where a jet mimics the photon. To suppress this background, the following photon isolation and shower shape requirements are applied:

- Energy deposited in HCAL within a cone of $\Delta R = 0.4$ around the photon direction must be $< 0.05\ E_{\gamma}$ or < 2.4 GeV;
- Energy deposited in ECAL within a cone of $\Delta R = 0.4$ around the photon direction, excluding the energy associated to the photon, must be $< 0.05\ E_{\gamma}$ or < 3 GeV;
- Number of tracks in a cone of $\Delta R = 0.35$ around the photon direction must be < 3, and the total p_{T} of the tracks must be $< 0.1\ p_{\mathrm{T}}^{\gamma}$.
- The photon cluster major and cluster minor must be in the range of 0.15-0.35, and 0.15-0.3, respectively. Cluster major and minor are defined as second moments of the energy distribution along the direction of the maximum and minimum spread of the ECAL cluster.

The distribution of the selected photon p_{T}^{γ} is shown in Figure 11 (left). The sample is understood to have significant contamination from QCD dijet background with a jet faking photon. However, to pass the above photon isolation and cluster shape requirements, a jet has to fluctuate to a leading π^0 (with $\pi^0 \to \gamma\gamma$) that is surrounded by very low hadronic activity. These fake "photons" have a scale similar to the real prompt photons, and therefore can serve as valid reference objects for the calibration purpose.

In the selected photon sample, we require the presence of a barrel jet ($|\eta| < 1.3$) recoiling against the photon candidate in azimuth by $\Delta\phi > 2/3\pi$. Figure 11 (right) shows the distribution of azimuthal angle between the photon and the leading jet before the $\Delta\phi$ cut is applied. To reduce the effect of initial and final state gluon radiation that violates jet-photon p_{T} balance, events containing additional jets with $p_{\mathrm{T}}^{\mathrm{jet2}} > p_{\mathrm{T,max}}^{\mathrm{jet2}}$ and outside the ΔR=0.25 cone around the photon direction are vetoed. Currently we use $p_{\mathrm{T,max}}^{\mathrm{jet2}} = 0.5\ p_{\mathrm{T}}^{\gamma}$ value, which is a very loose veto requirement, and is meant to preserve the data statistics.

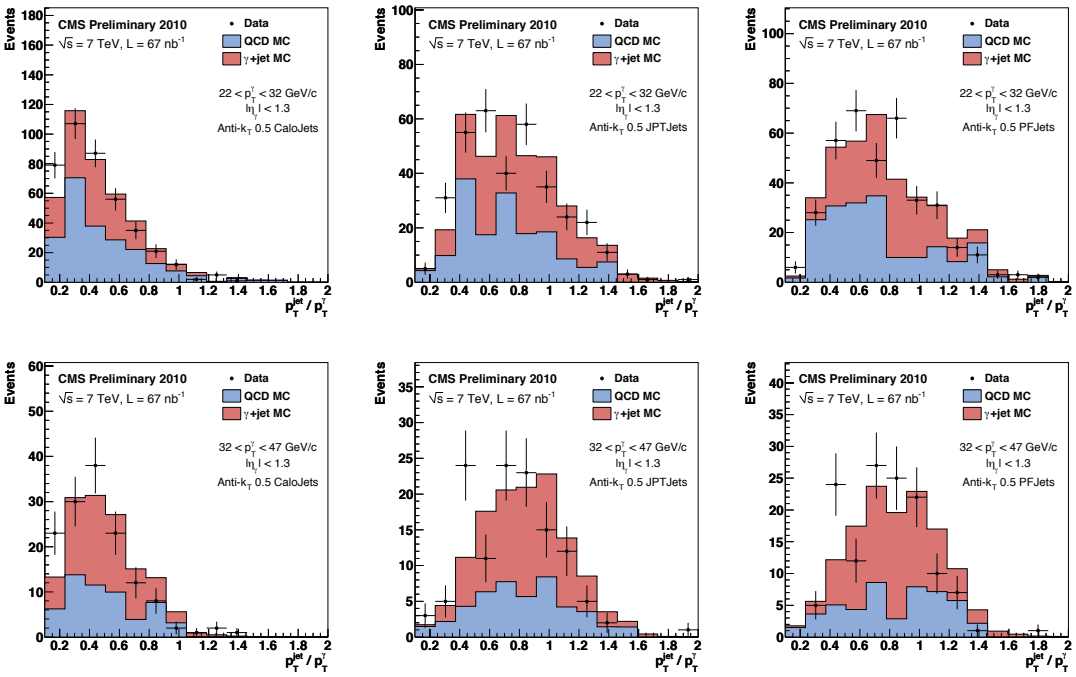

Figure 12: Distributions of $p_{\mathrm{T}}/p_{\mathrm{T}}^{\gamma}$ in data and MC for calorimeter (left), JPT (middle) and PFlow (right) jets in two representative p_{T}^{γ} bins.

The selected γ+jet calibration samples contain 1510, 1346, 1468 events for calorimeter, JPT and PFlow jets respectively. In these events we study the distributions of the response-sensitive variable $p_{\mathrm{T}}/p_{\mathrm{T}}^{\gamma}$ in bins of p_{T}^{γ}. The distributions are shown in Figure 12 for data and MC in two representative p_{T}^{γ} bins. Figure 13 shows the average response, extracted as the mean of the $p_{\mathrm{T}}/p_{\mathrm{T}}^{\gamma}$ distributions, versus p_{T}^{γ} for data and MC. It also displays data/MC ratio and the $\pm 5\%$ and $\pm 10\%$ uncertainty lines. For all three jet types, data/MC points are typically within $\pm 10\%$ uncertainty lines. One-parameter linear fits to the data/MC points give the parameter values of 0.928 ± 0.019, 0.919 ± 0.017, 0.926 ± 0.017 and χ^2/ndf of 2.79/5, 6.95/5, 4.00/5, for calorimeter, JPT and PFlow jets, respectively. Finally, Figure 13 also shows the true jet response obtained from γ+jet MC events, as a mean value of the p_{T} ratio of reconstructed jet and its spatially matched generator jet, $< p_{\mathrm{T}}^{Jet}/p_{\mathrm{T}}^{GenJet} >$. As can be seen, the jet response extracted from the γ+jet balancing exhibits sizable negative bias, compared to the true jet response, especially for JPT and PFlow jets. This effect is currently expected, and is attributed to the presence of additional jets in the event (below $p_{\mathrm{T,max}}^{\mathrm{jet2}}$ threshold) which spoil the idealized topology of a jet recoiling against a photon with exactly compensating transverse momenta, and thus leads to the lower observed values of $< p_{\mathrm{T}}/p_{\mathrm{T}}^{\gamma} >$. With higher data statistics we will be able to decrease the measurement bias by tightening the $p_{\mathrm{T,max}}^{\mathrm{jet2}}$ threshold on additional jets. Furthermore, large datasets will allow to measure the response for series of decreasing values of the $p_{\mathrm{T,max}}^{\mathrm{jet2}}$. The unbiased response then will be extracted by extrapolating the measurements to $p_{\mathrm{T,max}}^{\mathrm{jet2}}$ =0 level. However, in spite of the current bias in the absolute response measurement, observed agreement between data and MC when the same p_{T} balance method is applied indicates that the simulation describes detector response with reasonable precision.

We now turn to MPF method which starts from the simple assumption that the γ+jet events have no intrinsic missing E_T and that the photon is perfectly balanced by the hadronic recoil in the transverse plane:

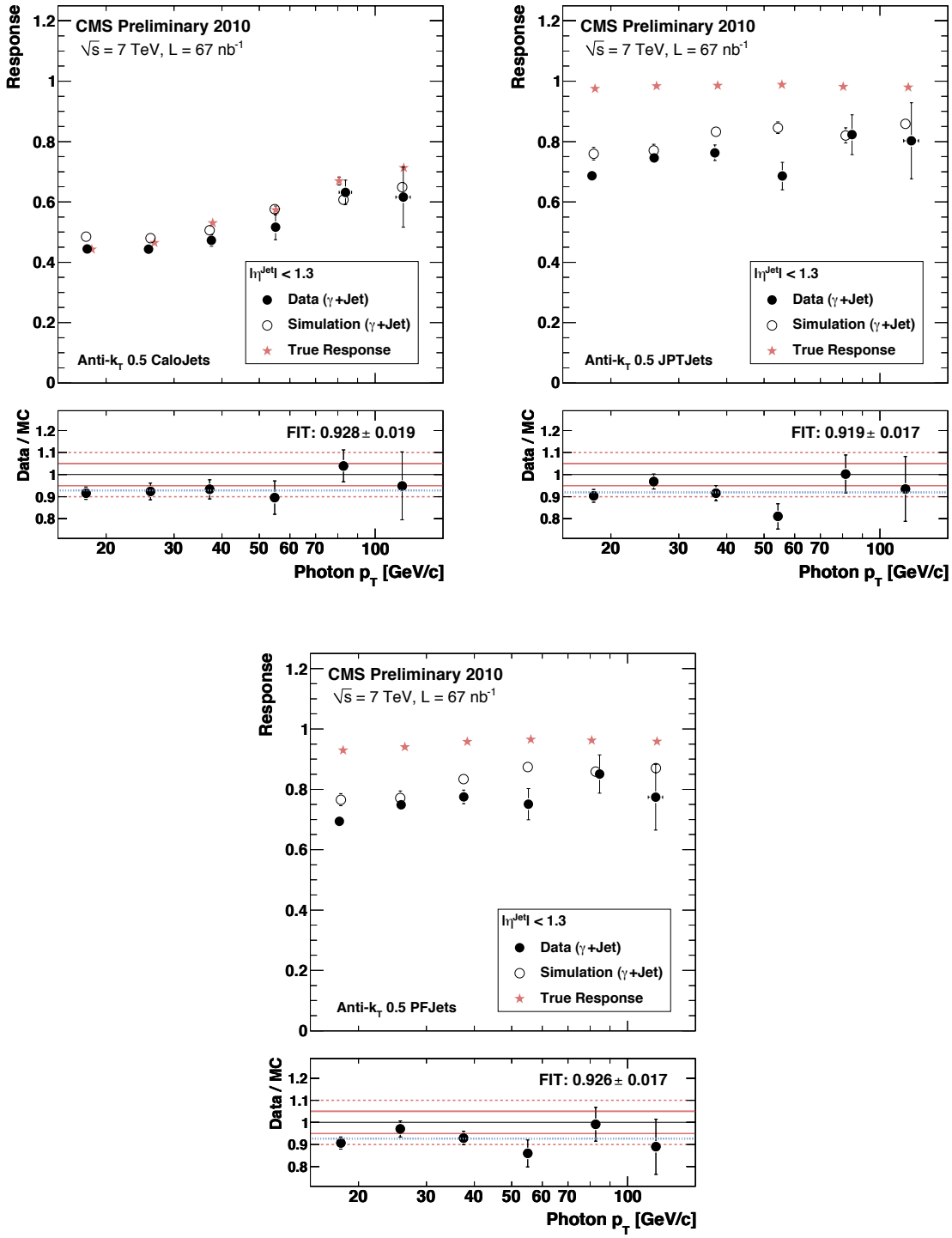

Figure 13: Response $< p_{\mathrm{T}}/p_{\mathrm{T}}^{\gamma} >$ versus p_{T}^{γ} in data and MC for calorimeter (top-left), JPT (top-right) and PFlow (bottom) jets. MC truth response is also shown. Data/MC ratio and the one-parameter linear fit function is shown at the bottom of the plots, together with $\pm$5% and$\pm$10% lines.

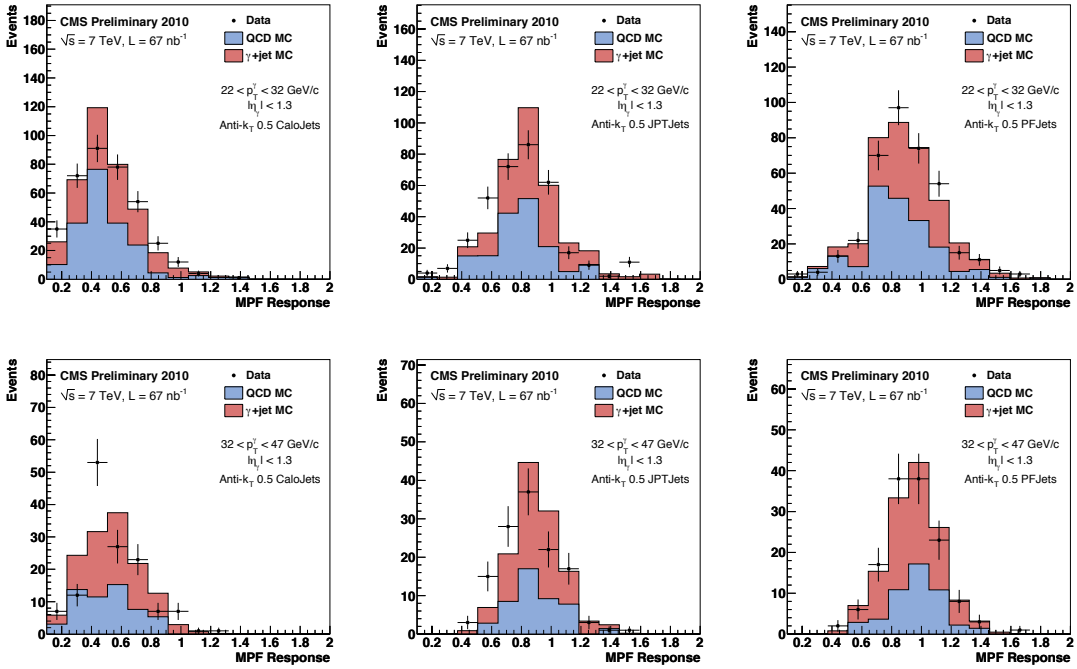

Figure 14: Distributions of MPF response in data and MC for calorimeter (left), JPT (middle) and PFlow (right) jets in two representative p_{T}^{γ} bins.

$$\vec{p_{\mathrm{T}}}^{\,\gamma} + \vec{p_{\mathrm{T}}}^{\,recoil} = 0 \tag{6}$$

For reconstructed objects, this equation can be rewritten as

$$R_{\gamma}\vec{p_{\mathrm{T}}}^{\,\gamma} + R_{recoil}\vec{p_{\mathrm{T}}}^{\,recoil} = -\vec{E}_T^{miss} \tag{7}$$

where R_{γ} and R_{recoil} are detector response to the photon and the hadronic recoil. Assuming well calibrated photon, $R_{\gamma} = 1$, solving the two equation for R_{recoil} gives:

$$R_{recoil} = 1 + \frac{\vec{E}_T^{miss} \cdot \vec{p_{\mathrm{T}}}^{\,gamma}}{(p_{\mathrm{T}}^{\gamma})^2} \equiv R_{MPF} \tag{8}$$

This equation forms the definition of MPF response R_{MPF}. The extra step needed to identify MPF response with the true jet response is $R_{recoil} = R_{leadjet}$. However, it is not strictly necessary that the recoil consists of only one jet, response of which we are trying to measure. $R_{recoil} = R_{leadjet}$ holds to a good approximation if particles not clustered into the leading jet have a response similar to the ones inside the jet, or these particles are in direction perpendicular to the photon axis. Small response differences are tolerated as long as most of the recoil is clustered into the leading jet. This is ensured by $p_{\mathrm{T}}^{\mathrm{jet2}} < p_{\mathrm{T,max}}^{\mathrm{jet2}}$ cut and $\Delta\phi$ cut between the leading jet and the photon in the selected γ+jet sample. For consistency, the jet and the missing E_T are reconstructed using the same constituent types. The MPF method has been extensively used at the Tevatron [14].

Distributions of MPF response in the selected γ+jet calibration sample are shown in Figure 14 for the same respresentative $p_{\mathrm{T}}{}^{\gamma}$ bins as in the case of the p_{T} balancing method. We observed

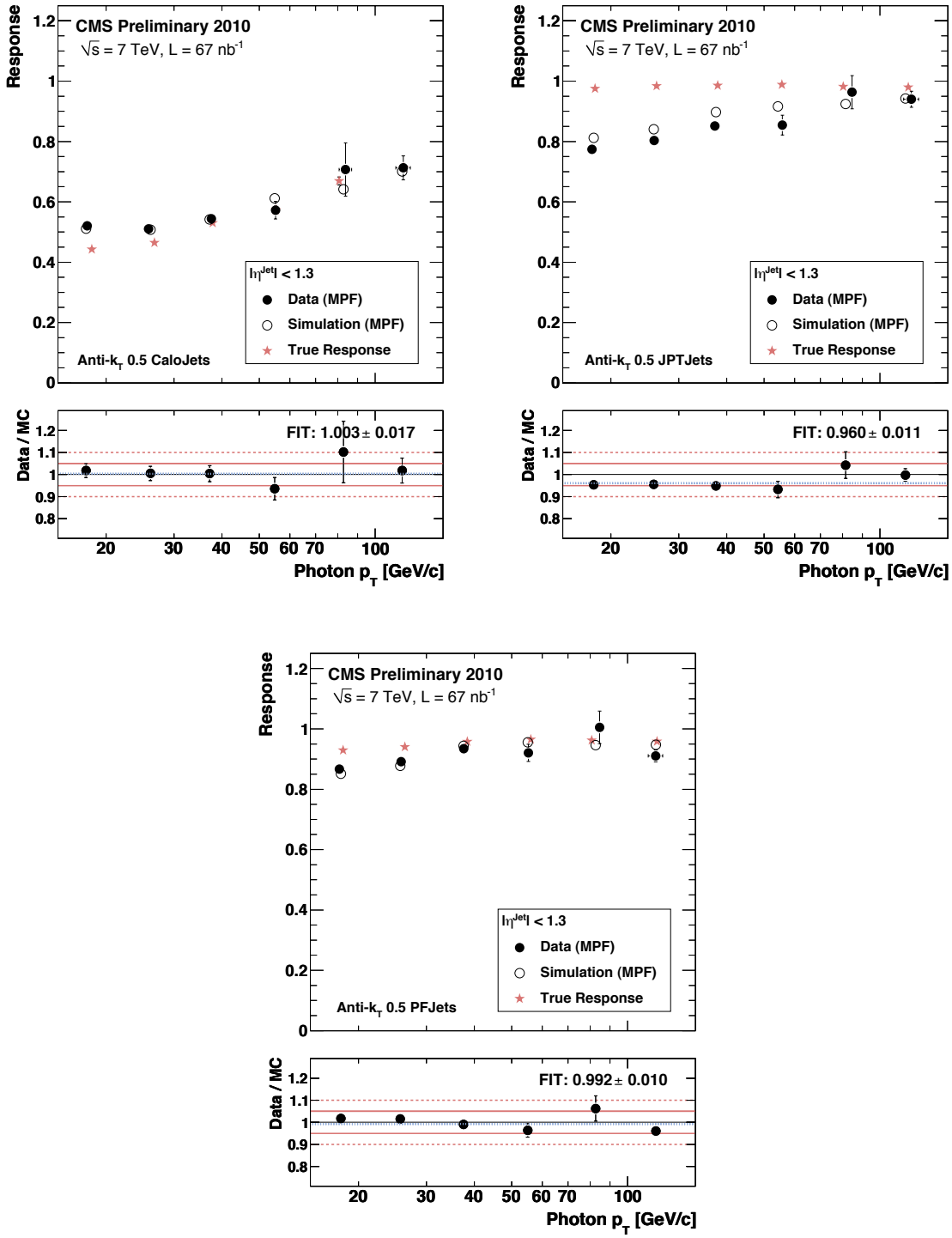

Figure 15: MPF response in data and MC for calorimeter (top-left), JPT (top-right) and PFlow (bottom) jets. MC truth response is also shown. Data/MC ratio and the one-parameter linear fit function is shown at the bottom of the plots, together with $\pm 5\%$ and $\pm 10\%$ lines.

that MPF response distributions are much narrower compared to p_T balancing response (Figure 12). As explained earlier, this is because MPF method is less affected by event-by-event fluctuations from the secondary jets in event, as long as these jets have response similar to the leading one.

Figure 15 shows the average MPF response versus p_T^γ for data and MC. It also displays data/MC ratio and the $\pm$5% and $\pm$10% uncertainty lines. For all three jet types, data/MC points are typically within $\pm$5% uncertainty lines. One-parameter linear fits to the data/MC points give the parameter values of 1.003$\pm$0.017, 0.960$\pm$0.011, 0.992$\pm$0.010 and χ^2/ndf of 2.57/5, 4.60/5, 6.66/5, for calorimeter, JPT and PFlow jets, respectively. Figure 15 also shows the true jet response obtained from γ+jet MC events, as a mean value of the p_T ratio of reconstructed jet and its spatially matched generator jet, $< p_T^{Jet}/p_T^{GenJet} >$. We see that MPF response agrees better with the true response, than p_T balancing response does. This is again explained by less sensitivity of the MPF method to the presence of secondary jets in the event.

Observed agreement between data and MC when the same MPF method is applied indicates that the simulation describes detector response within 5% precision.

5 Jet p_T and position resolutions

The precise knowledge of the jet p_T and position resolutions is an important ingredient to many analyses considering jets in the final state, in order to relate measured quantities to the true properties of the underlying processes. Examples include usage of jet p_T resolution as a function of the jet transverse momentum to unfold differential jet spectra, and employing precise description of non-Gaussian tails in p_T resolution to predict missing transverse energy tails from QCD jet production that presents dominant background to many new physics searches.

In the following sections we present results on jet p_T and position resolutions as extracted from MC truth information, and measured directly from the collider data. Unless stated otherwise, Calorimeter, PFlow and JPT jets in all of these studies are corrected for the jet energy scale with correction factors derived from MC simulation as described in Section 4.1.

5.1 Monte Carlo truth jet p_T resolution

Jet energy resolution derived from simulation based on MC truth serves as a benchmark for measurements of the jet resolution derived directly from collision data samples, e.g. using the dijet asymmetry method discussed in the following sub-section.

To extract jet resolutions from simulation data, we use PYTHIA QCD dijet MC events, where we reconstruct calorimeter, JPT and PFlow jets, as well as generator jets. The latter serve as reference objects. They are unambiguously matched to reconstructed jets (calorimeter, JPT, or PFlow jets) by requiring $\Delta R < \Delta R_{\rm max}$. We use $\Delta R_{\rm max}$ =0.2 in general, except that $\Delta R_{\rm max}$ =0.1 for JPT (PFlow) jets in $|\eta|$ <2 ($|\eta|$ <2.5) region. The latter $\Delta R_{\rm max}$ values are motivated by better position resolutions of jets which incorporate tracking. Beyond $|\eta|$ =2 (2.5), JPT (PFlow) jets rely on calorimeter information only, and thus the same $\Delta R_{\rm max}$ =0.2 matching is used here as for the calorimeter jets. The choice of the matching distance $\Delta R_{\rm max}$ affects the widths of the response distributions at low p_T, but has negligible effect for $p_T > 40$ GeV. The values we use here yield approximately the same matching efficiencies for all three jet types, and are intended for a fair comparison of resolutions for well-matched jets of different types. Only the two matched pairs with the highest transverse momentum generator jets are considered. The jet response for each pair is defined as $p_T/p_T^{\rm REF}$ where p_T and $p_T^{\rm REF}$ refer to the transverse momenta of the reconstructed jet and its matched reference generator jet respectively. The

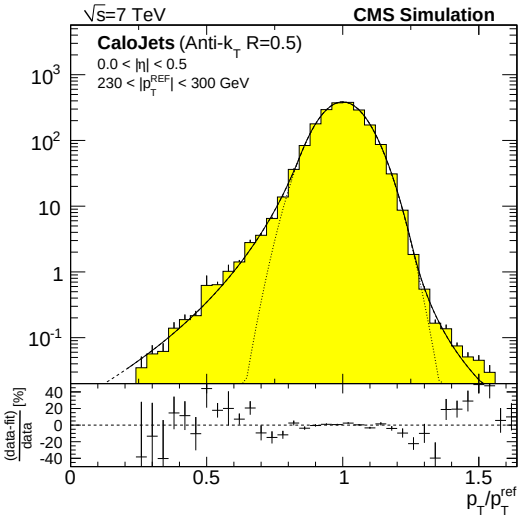

Figure 16: Distribution of calorimeter jet response, $p_{\mathrm{T}}/p_{\mathrm{T}}^{\mathrm{REF}}$, in MC simulation for a particular $|\eta|$ and $p_{\mathrm{T}}^{\mathrm{REF}}$ range. Example of fit with Gaussian and double-sided Crystal Ball are shown. The residuals in percent with respect to the latter are shown at the bottom.

width of the jet response distribution, in a given $|\eta|$ and $p_{\mathrm{T}}^{\mathrm{REF}}$ bin, is interpreted as the jet resolution. Figure 16 shows example of $p_{\mathrm{T}}/p_{\mathrm{T}}^{\mathrm{REF}}$ distribution for calorimeter jets in $|\eta|$ <0.5 and with 230 GeV< $p_{\mathrm{T}}^{\mathrm{REF}}$ < 300 GeV.

The MC-truth jet resolution can, in good approximation, be described by the σ of a Gaussian fit to the core of the jet response distribution. This is a robust description, relying on a single parameter (σ), and should be sufficient for many if not most applications in physics analysis. Some use cases however require an accurate description of the non-Gaussian tails. We therefore additionally apply Double Crystal Ball fits, describing the low and high tails by a power law. Figure 16 shows both the Gaussian and double-sided Crystal-Ball fits overlaid on $p_{\mathrm{T}}/p_{\mathrm{T}}^{\mathrm{REF}}$ distribution. While a Gaussian describes well the core of the distribution, a double-sided Crystal-Ball fit is a more accurate representation of the entire shape. The p_{T} dependencies of the jet resolutions extracted as Gaussian widths are shown in Figure 17 for the three types of jets in four representative η ranges. We observe a different behavior of JPT and PFlow jets, and their improved resolutions compared to calorimeter jets, due to the incorporation of tracking information; this effect is especially pronounced at p_{T} below ∼200 GeV and for the region of pseudorapity where the tracking information is employed. In forward region beyond $|\eta|$=2.5, the resolutions of calorimeter, JPT and PFlow jets are very similar, as expected.

An example where the Gaussian description is not sufficient, is a search for physics beyond standard model in events with multiple jets and a large missing E_T^{miss} due to stable weakly interacting particles that escape detection. Main background to this signal is expected from QCD multijet production where E_T^{miss} can originate from fluctuations in the detector response to hadronic showers. One way to estimate the QCD background in the high E_T^{miss} signal region is to smear well-balanced multijet events with parametrizations of the full jet energy resolution functions that model both the Gaussian core and the tails of the response distributions. We are developing data-driven methods to measure the full resolution functions in γ+jet and dijet samples. These methods require more data statistics than currently available from LHC collisions, but are being tested on MC samples and indicate good future potential.

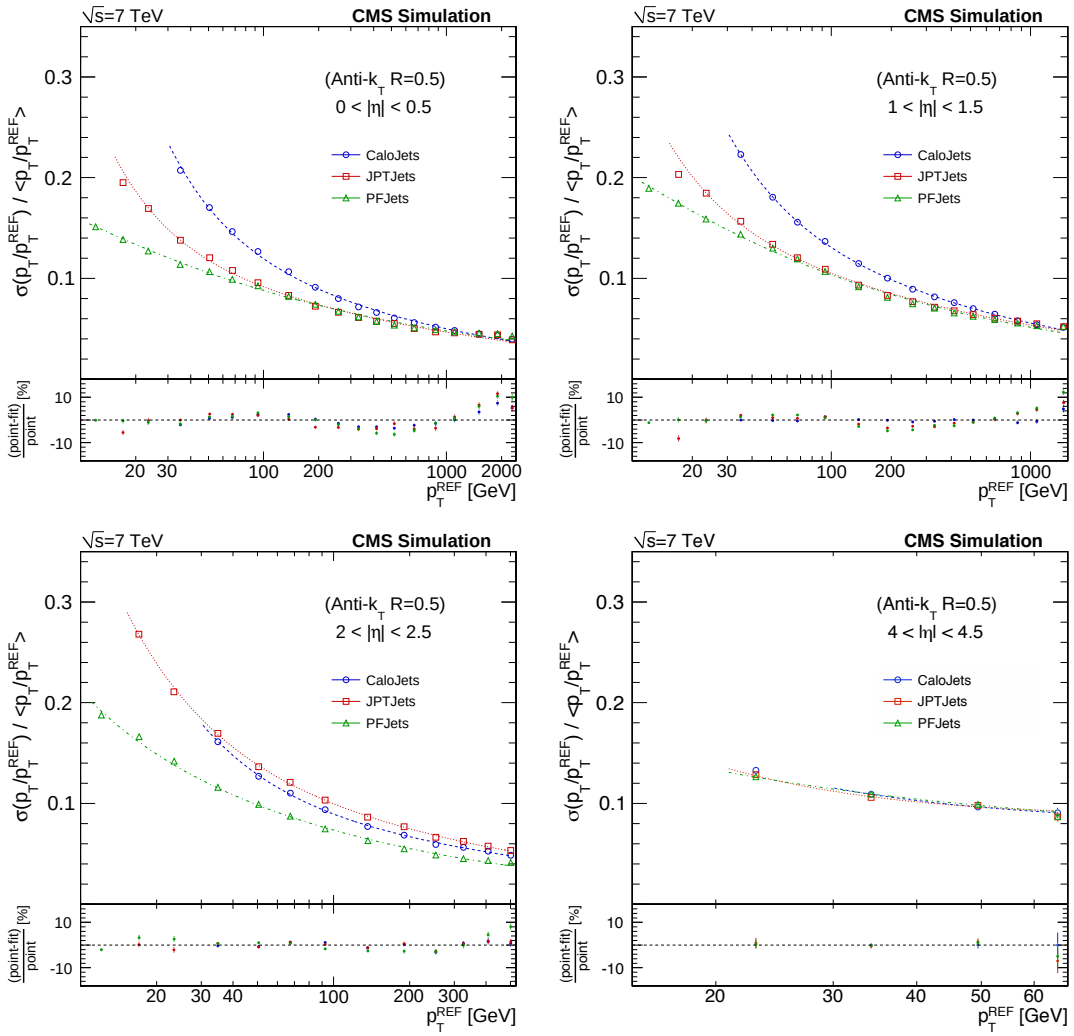

Figure 17: Jet p_T resolution (Gaussian σ) as a function of p_T^{REF} for four representative $|\eta|$ ranges.

5.2 Jet p_T resolutions from dijet asymmetry method

The asymmetry method described in this section allows jet p_T resolution measurement directly from collision data. The method exploits momentum conservation in the transverse plane of dijet system and is based (almost) exclusively on the measured kinematics of the dijet events. It was first developed at the DØ experiment at the Tevatron [19] and recently established at CMS for calorimeter jets based on simulation studies [20].

To collect the dijet sample, we use Minimum Bias and dijet p_T average triggers (with 15 GeV and 30 GeV thresholds), the latter being the same triggers as the ones used in the relative jet response measurement (Section 4.2.2). Integrated luminosity for the unprescaled dijet p_T average trigger with 30 GeV threshold corresponds to $L_{int} = 73\ \text{nb}^{-1}$.

At offline, events are required to contain at least two jets within $|\eta|$ <1.4, with the leading jet pair being azimuthally separated by $\Delta\phi > 2.7$. Any additional third jet in event is required to have low uncorrected transverse momentum $p_T^{jet3} < p_{T,max}^{jet3}$. We define asymmetry variable

$$A = \frac{p_T^{jet1} - p_T^{jet2}}{p_T^{jet1} + p_T^{jet2}} \tag{9}$$

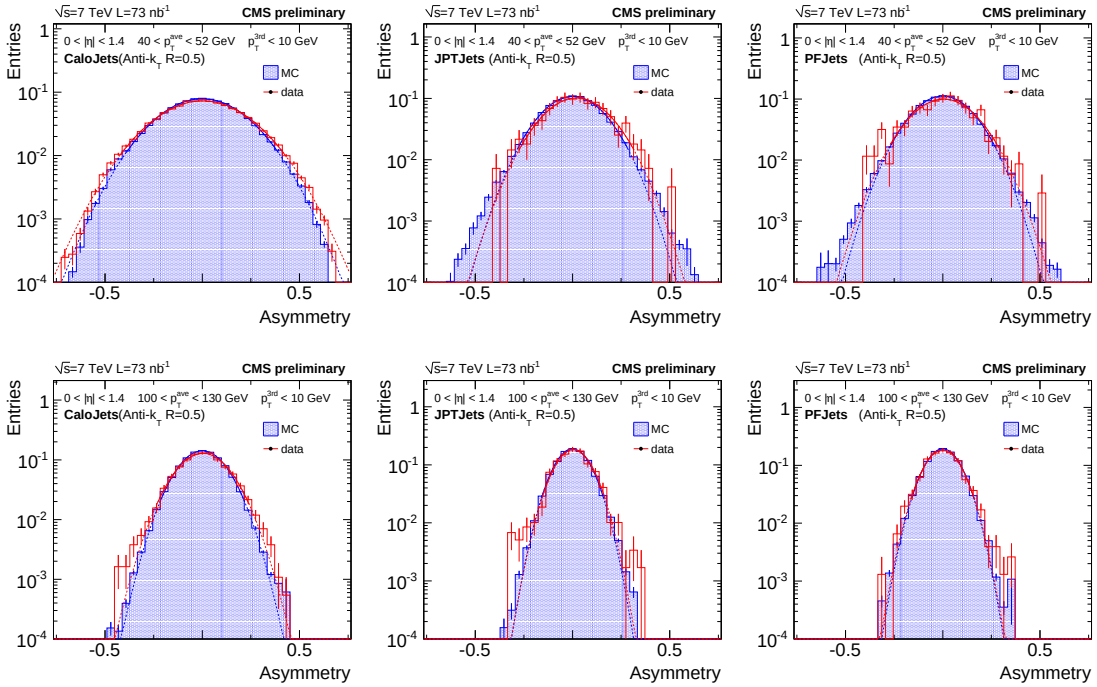

Figure 18: Distributions of asymmetry variable A in two representative p_T^{ave} bins for calorimeter (left) and JPT (middle) and PFlow (right) jets.

where p_T^{jet1} and p_T^{jet2} refer to the randomly ordered transverse momenta of the two leading jets. For approximately equal values of p_T of both jets, and their resolutions, the variance of the asymmetry σ_A can be related to the jet p_T resolution as:

$$\frac{\sigma(p_T)}{p_T} = \sqrt{2}\sigma_A \,. \tag{10}$$

Figure 18 shows examples of asymmetry variable distributions for the three jet types in two representative bins of $p_T^{ave} \equiv (p_T^{jet1} + p_T^{jet2})/2$. Distributions from data are compared to the MC expectations. The latter are extracted from PYTHIA QCD dijet events passed through the same analysis chain. The distributions exhibit reasonable data/MC agreement.

Jet p_T resolutions extracted from the dijet asymmetry distributions are understood to be overestimated. This is because the presence of additional soft radiation spoils the idealized topol-

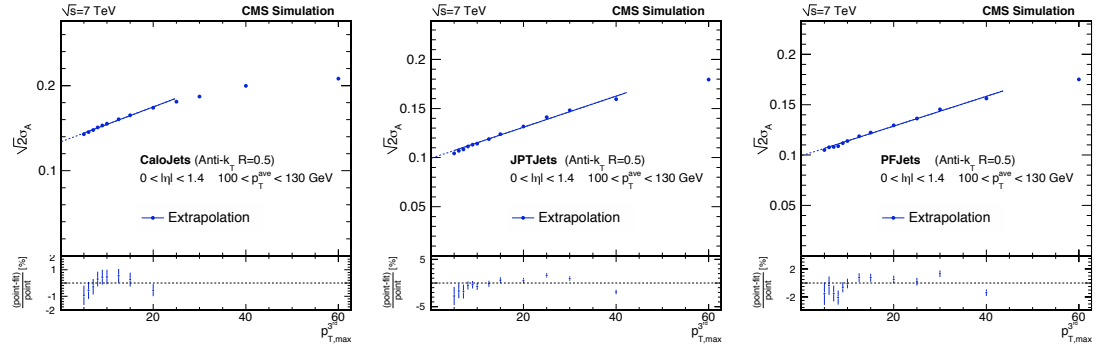

Figure 19: Examples of extrapolation of $\sqrt{2}\sigma_A$ as a function of $p_{T,max}^{jet3}$ to zero, for calorimeter (left) and JPT (middle) and PFlow (right) jets for $100 < p_T^{ave} < 130\,\text{GeV}$ and $0 \leq |\eta| < 1.4$ bin.

ogy of two jets with exactly compensating transverse momenta, and thus broadens the asymmetry distributions. To account for this effect, the measurement of the asymmetry in each bin of p_T^{ave} is carried out multiple times for decreasing value of $p_{T,max}^{jet3}$. The corrected resolution is then extracted by extrapolating measurements to $p_{T,max}^{jet3} = 0$ value. The extrapolated curves are illustrated in Figure 19 for a particular bin of p_T^{ave}.

In addition to the discussed soft radiation effects, there are other physics effects that broaden the dijet asymmetry distribution: part of the event transverse momentum is taken by the proton remnants in the form of underlying event energy; and parton showering and hadronization result in some particles emitted outside the jet cones. These effects are unrelated to the detector resolution, as they cause the dijet asymmetry smearing even at the level of particle jets. To account for this particle-level imbalance contribution to the measured jet p_T resolution, the asymmetry method is applied to GenJets and the observed particle level-resolution is subtracted in quadrature from the measurement.

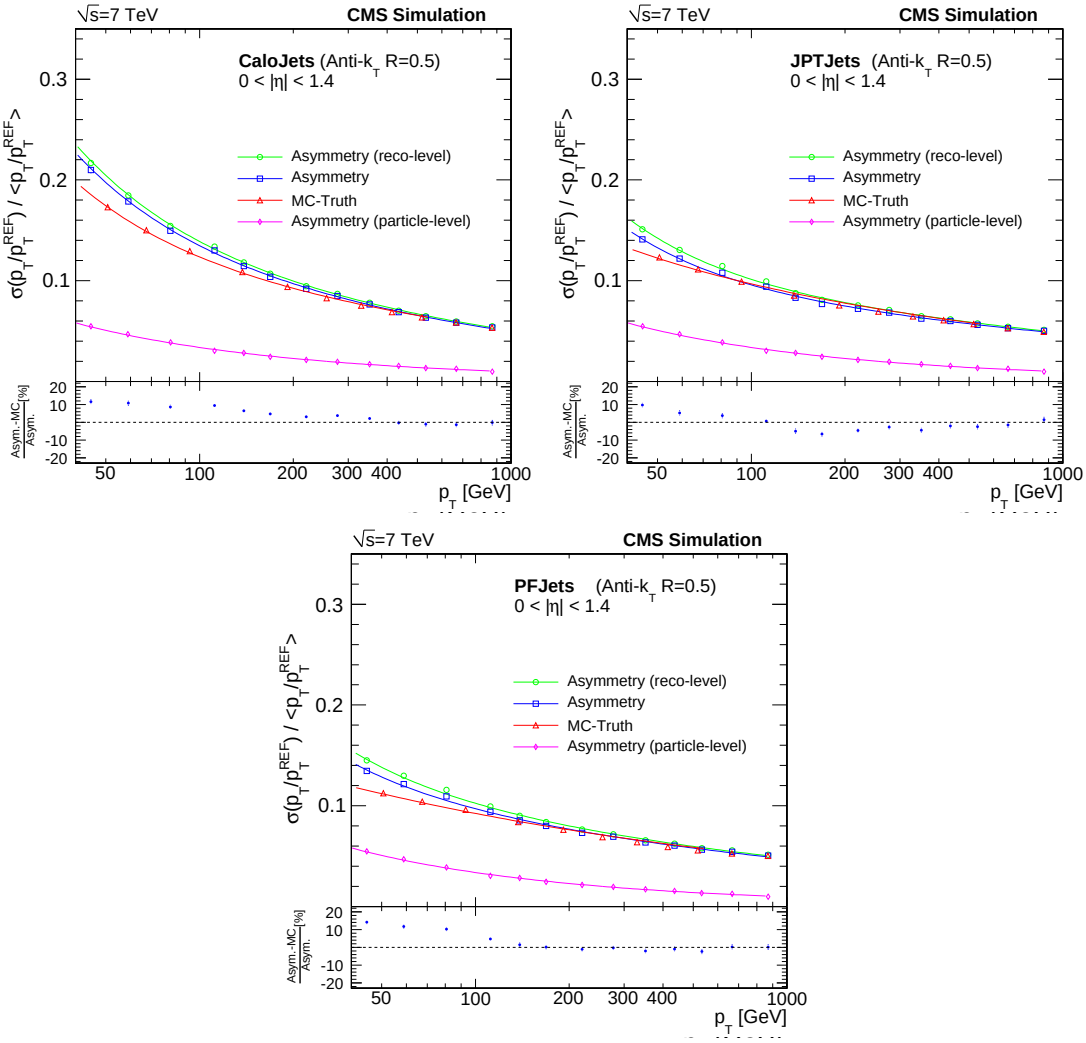

Figure 20: Application of the asymmetry method to simulated calorimeter (top left), JPT (top right) and PFlow (bottom) jets for $0 \leq |\eta| < 1.4$. The reco- (blue) and particle-level (magenta) results are shown together with the final measurement (green) and a comparison to the MC truth derived resolution (red).

The asymmetry method is first validated using PYTHIA QCD dijet events. This is illustrated in Figure 20 which shows the different steps of the asymmetry procedure for calorimeter, JPT and PFlow jets respectively. For each jet type, the "raw" jet resolution from the asymmetry method, including the extrapolation of $p_{T,max}^{jet3}$ to zero, is shown in green. It is corrected by subtracting in quadrature the estimation of the intrinsic particle level resolution, shown in magenta, as obtained from the application of the dijet asymmetry method to GenJets. This final resolution from the asymmetry method is shown in blue. It is compared to the resolution estimate from MC truth (described in Section 5.1) shown in red. We see that the resolutions obtained from the data-driven method of dijet asymmetry reproduce the MC truth results above $p_T^{ave} > 40\,GeV$ for all types of jets within a 10% deviation.

The full asymmetry analysis procedure is then applied to the selected data sample, and the obtained jet p_T resolutions are shown in Figure 21 for the three jet types. The figure also shows results from PYTHIA QCD dijet sample obtained with the dijet asymmetry method, and the data/MC ratio. While still limited by the size of the available data sample, data and simulation are in reasonable agreement, typically at 10 % level. As expected, the resolutions for jets

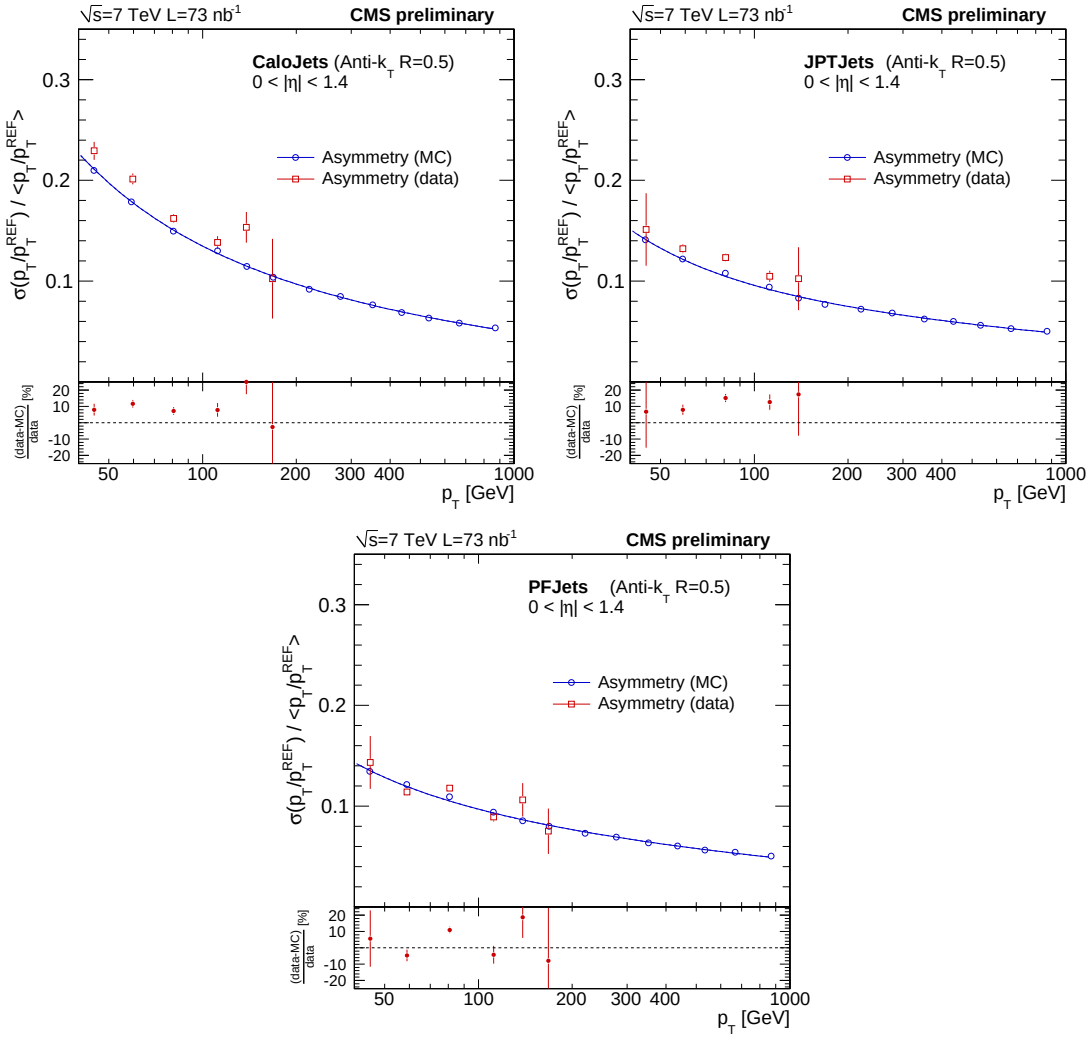

Figure 21: Calorimeter (top left), JPT (top right) and PFlow (bottom) jet resolution for $0 \leq |\eta| < 1.4$ determined with the asymmetry method from QCD simulation and compared with the result from data using the same procedure.

employing tracking information are improved compared to the calorimeter jets.

5.3 Jet position resolutions

The knowledge of jet position resolutions is important for many physics analyses, e.g. for unfolding of quantities measured from jet positions. We derive jet position resolutions (η and ϕ) from Monte Carlo simulation, and perform a validation study with early collision data.

To derive jet position resolutions from simulation, we use PYTHIA QCD dijet MC sample. In these events we match GenJets, which serve as reference, and the corresponding reconstructed jets (calorimeter, JPT, PFlow or track jets) by requiring $\Delta R < 1.0$ for the closest match. Only dijet events with a $\Delta\phi(jet1, jet2) > 2.0$ and only the two leading jets are considered. Such loose requirements are used to reduce any bias on the determination of the position resolution from the position-matching procedure. For each of these jets the differences of GenJet position and reconstructed jet position are calculated as follows: $\Delta\eta = (\eta - \eta_{ref})\,\mathrm{sign}(\eta_{ref})$, and $\Delta\phi = \phi - \phi_{ref}$ ($\Delta\eta$ includes the sign of η_{ref} to account for a small asymmetric offset while binning in $|\eta_{ref}|$).

Each $\Delta\eta$ and $\Delta\phi$ distribution in individual bins of p_T and η is characterized by a Gaussian core and small exponential tails. The p_T dependence of the Gaussian core resolutions is presented in Figs. 22 and 23 for calorimeter, JPT, PFlow and track jets. We see improved position resolutions for the jet types employing tracking, with PFlow jets displaying the best performance.

In order to validate the simulation-based results on the jet position resolutions at central η, we select back-to-back dijet sample in $L_{int} = 8.4$ nb^{-1} data, and study the relative $\Delta\eta$ and $\Delta\phi$ of calorimeter jets with respect to track jets, and with respect to PFlow jets, using the same matching procedure as described above in case of GenJets. Since calorimeter jets and track jets are measured from independent detector components, this comparison allows to validate the calorimeter jet resolution under the assumption of a smaller (and well modeled) track jet resolution. Calorimeter jet and PFlow jet reconstruction is partially correlated but comparing their relative position measurements further supports the validation of calorimeter jets, since PFlow jets are observed to have the best position resolution. The widths of the distributions of the relative positions as a function of jet p_{T} are shown in Fig. 24 for data and MC, for $|\eta| <$0.5 range. We see reasonable data/MC agreement indicating that the CMS simulation gives reliable description of the jet position resolutions.

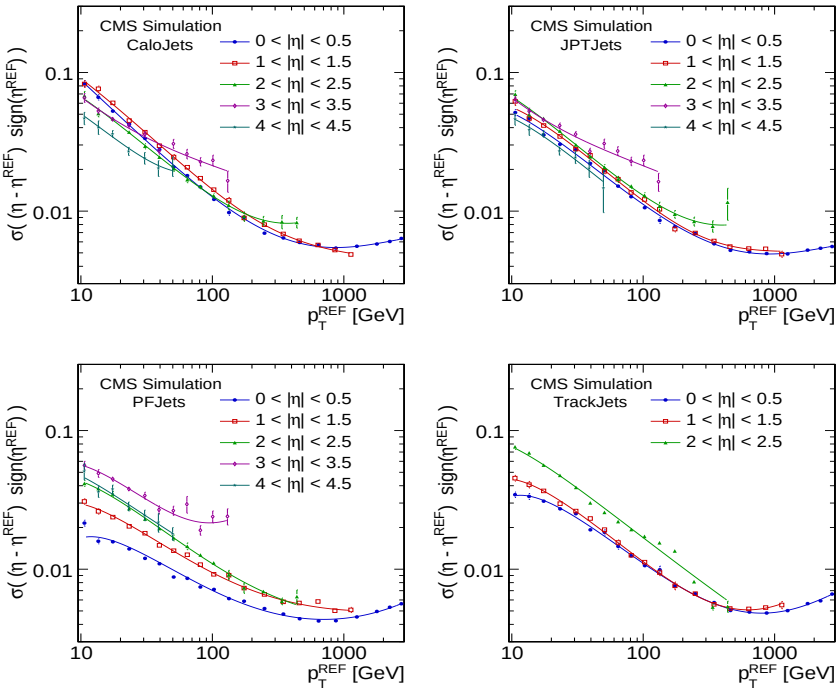

Figure 22: MC-truth jet η resolutions for calorimeter (top left), JPT (top right), PFlow (bottom left) and track jets (bottom right).

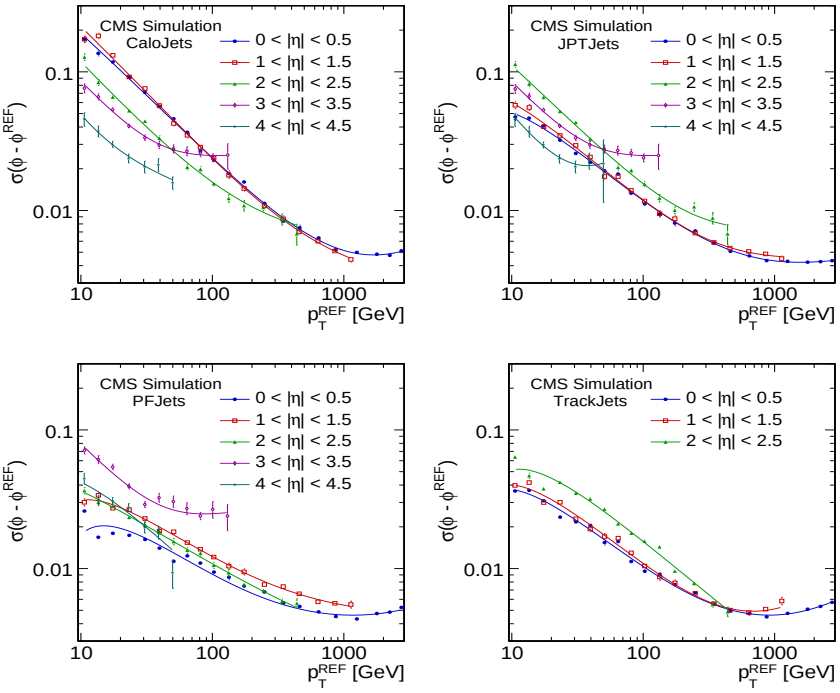

Figure 23: MC-truth jet ϕ resolutions for calorimeter (top left), JPT (top right), PFlow (bottom left) and track jets (bottom right).

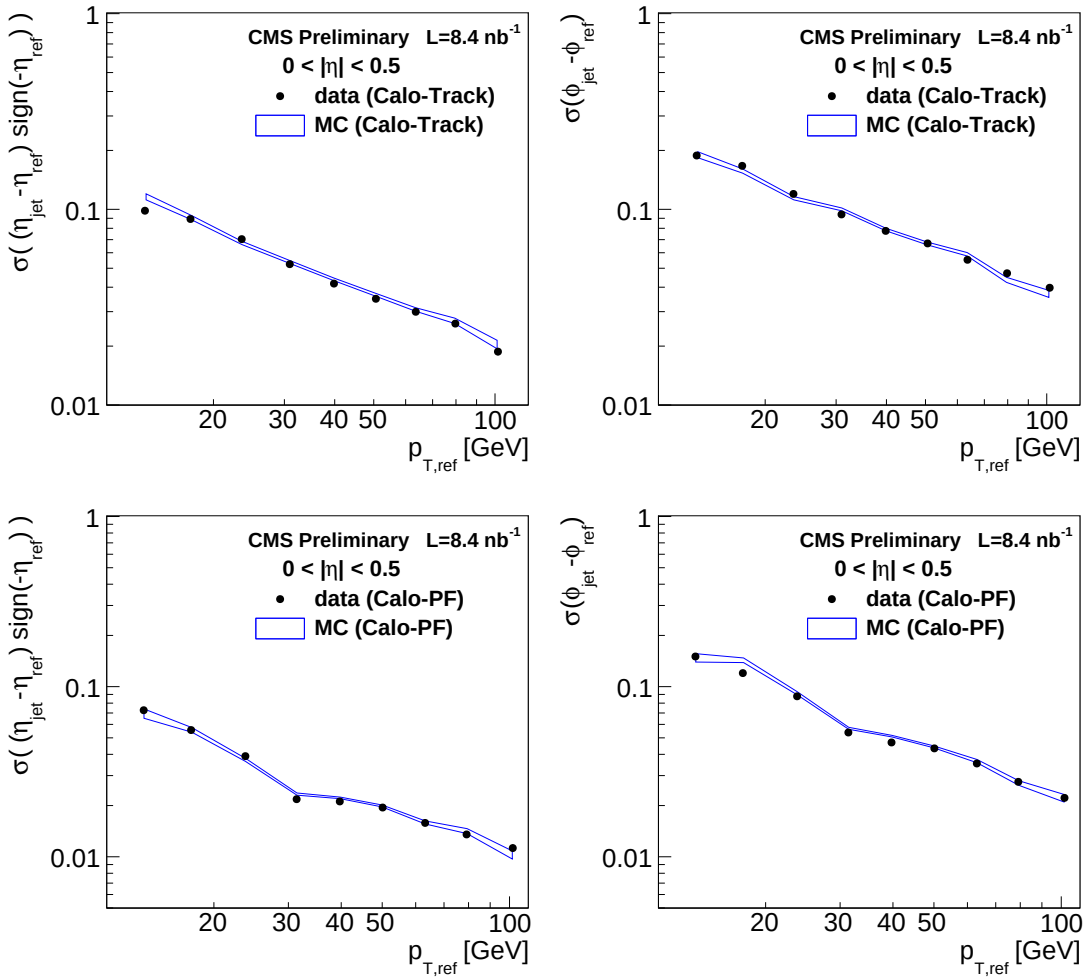

Figure 24: $\sigma(\Delta\eta)$ (left) and $\sigma(\Delta\phi)$ (right) in data and Monte Carlo of calorimeter jets with respect to track jets (top) and PFlow jets (bottom).

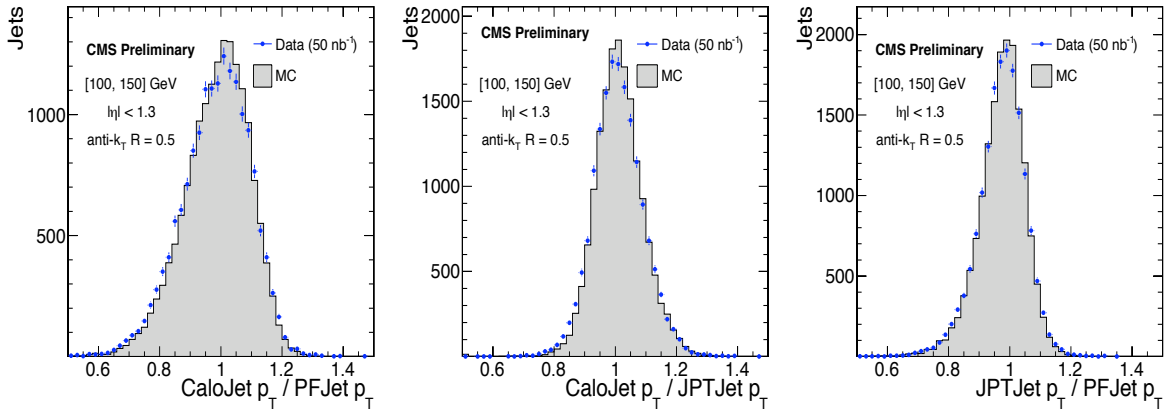

Figure 25: Distributions of p_T ratios between spatially matched different types of jets: calorimeter jet p_T/PFlow jet p_T (left), calorimeter jet p_T/JPT jet p_T (middle) and JPT jet p_T/PFlow jet p_T (right).

6 Jet energy scale and resolution uncertainties and jet-by-jet comparison between different jet types

Current physics analyses in CMS use 10% (5%) JEC uncertainties for calorimeter jets (JPT and PFlow jets), with the additional 2% uncertainty per unit rapidity. Results from the current limited statistics dataset, presented in sections 4.2.1-4.2.3, indicate that these are conservative uncertainty estimates. The 10% uncertainties are used for evaluation of the systematic errors due to the jet resolutions effects for all three jet types. Observations from the data, presented in Section 5.2, support this number as a reasonable estimate.

The in-situ jet calibration provides direct information about the uncertainty of the jet energy scale. It is, however, interesting to estimate this uncertainty from the fundamental considerations based on the precisions of measuring the underlying constituents inside a jet. PF jets, which are built starting from all reconstructed particles in an event, provide a natural environment for this kind of analysis. At low p_T, the scale of the transverse momentum of charged particles is known to much better than 1% [21], and the ECAL energy scale for electromagnetic objects is known to 1-3% [5, 22]. Studies of the calorimeter response to a single particle [5, 17] indicate 3-5% level agreement between data and simulation in the $|\eta| < 2.2$ region. For a PFlow jet at low p_T the energy deposits in the calorimeter of its constituents are well separated and

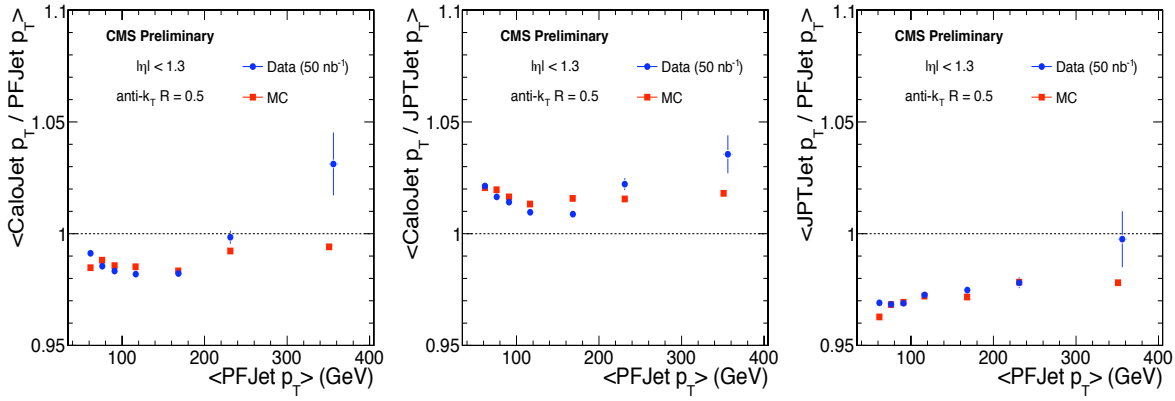

Figure 26: Relative calorimeter/PFlow (left), calorimeter/JPT (middle) and JPT/PFlow (right) jet response versus PFlow jet p_T.

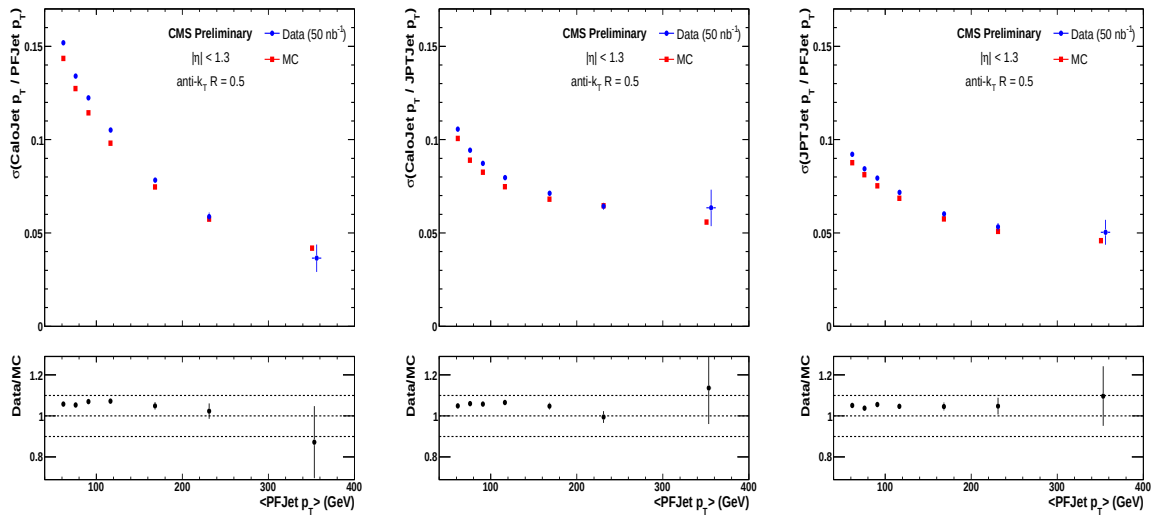

Figure 27: Relative calorimeter/PFlow (left), calorimeter/JPT (middle) and JPT/PFlow (right) jet resolutions versus PFlow jet p_{T}.

only the 10% of the energy carried by the neutral hadrons is measured with the 3-5% uncertainty. At high energy the constituents are less separated resulting in a larger fraction of the jet energy measured with the calorimeters only. Overall, one can expect that JEC uncertainty smaller than the currently used 5% estimate is achievable. Indications from the studies of photon+jets events, discussed in Section 4.2.3, support this conclusion.

Well measured PFlow jets can serve as reference objects for the other jet reconstruction types. To check the relative calibration of the three jet types in the barrel region ($|\eta|$ <1.3), we select dijet events in L_{int} =50 nb^{-1} of data, and perform a comparison on a jet-by-jet basis. PFlow, calorimeter and JPT jets are all corrected for their respective MC-truth JEC, and are matched spatially by requiring $\Delta R(Calo, PFlow)$ <0.25 and $\Delta R(Calo, JPT)$ <0.25 and $\Delta R(PFlow, JPT)$ <0.25. The simultaneous matching between all reconstruction types ensures an unambiguous jet identification. For the two matched jets with highest corrected PFlow jet transverse momentum in each event, the relative responses – calorimeter jet p_{T}/ PFlow jet p_{T}, calorimeter jet p_{T}/ JPT jet p_{T}, JPT jet p_{T}/ PFlow jet p_{T}– are recorded in bins of PFlow jet p_{T}. Representative distributions are shown in Figure 25. Despite the fact that the different jet reconstruction types require significantly different energy calibrations (as shown in Figure 1), the relative response of the various jet types peaks near unity after the calibration is applied. We also observe an overall good agreement between the data and the simulation which successfully reproduces the full response distribution shape. The arithmetic mean of the response distributions, as a function of the average PFlow jet p_{T}, is shown in Figure 26. It should be noted, that the small observed deviations (2-4%) of the mean response from unity are expected due to the finite resolution of the jet energy and the steeply falling jet p_{T} spectrum. The magnitude of the resolution bias effect is described very well by the simulation which agrees with the data to better than 1%. These observations further confirm that currently used 5-10% uncertainties for the jet energy scale can be viewed as conservative estimates.

The width of the response distributions, as a function of the average PFlow jet p_{T}, is shown in Figure 27 for data and simulation. The figure also shows data/MC ratio. We observe a reasonable data/MC agreement for the corresponding relative resolutions within a 10% deviation. This further supports the estimated uncertainty of 10% (Section 5.2) on the jet energy resolution.

7 Conclusions

We have presented the first studies of jet energy calibration and jet resolutions from early pp collisions recorded by CMS at $\sqrt{s} = 7$ TeV. Three different techniques to reconstruct jets in CMS have been considered: calorimeter jets, Jet-Plus-Track jets and Particle-Flow jets. Anti-k_{T} clustering algorithm with cone size of $R = 0.5$ has been used for all three types.

Following the approach of multi-step factorized jet energy calibration adopted by CMS, we have studied separately offset, relative and absolute jet energy corrections. Energy offset due to electronic noise and event pile-up has been estimated from Zero Bias and Minimum Bias trigger data. The dijet p_{T} balance has been used to measure the jet response as a function of pseudorapidity, relative to the central region ($|\eta|$ <1.3). The p_{T} balance and MPF methods in photon+jet events have been used to study the jet response in the central region as a function of jet p_{T}. Jet energy resolutions have been studied using asymmetry method in dijet data events. The sample has also been used to study jet position resolutions.

Significantly better performance for the jet types employing the tracking information have been observed compared to the jets using calorimeter-only information.

Current physics analyses in CMS use 10% (5%) JEC uncertainties for calorimeter jets (JPT and PFlow jets), with the additional 2% uncertainty per unit rapidity. Observations from the current limited statistics datasets support these numbers as conservative estimates. The 10% uncertainties are used for evaluation of the systematic errors due to the jet resolutions effects for all three jet types. Observations from the data support this number as a reasonable estimate.

References

[1] CMS Collaboration, "The CMS experiment at the CERN LHC", *JINST* **3** (2008) S08003. doi:10.1088/1748-0221/2/08/S08004.

[2] M. Cacciari, G. P. Salam, and G. Soyez, "The anti-kt jet clustering algorithm", *JHEP* **0804:063** (2008).

[3] CMS Collaboration Collaboration, "Jet Plus Tracks Algorithm for Calorimeter Jet Energy Corrections in CMS", *CMS PAS* **JME-09-002** (2009).

[4] CMS Collaboration, "Particle-Flow Event Reconstruction in CMS and Performance for Jets, Taus, and E_T^{miss}", *CMS PAS* **PFT-09-001** (2009).

[5] CMS Collaboration, "Commissioning of the Particle-Flow Reconstruction in Minimum-Bias and Jet Events from pp Collisions at 7 TeV", *CMS PAS* **PFT-10-002** (2010).

[6] CMS Collaboration, "Commissioning of TrackJets in pp Collisions at $\sqrt{s} = 7$ TeV", *CMS PAS* **JME-10-006** (2010).

[7] CMS Collaboration, "Tracking and Vertexing Results from First Collisions", *CMS PAS* **TRK-10-001** (2010).

[8] CMS Collaboration, "Calorimeter Jet Quality Criteria for the First CMS Collision Data", *CMS PAS* **JME-09-008** (2009).

[9] CMS, "Plans for Jet Energy Corrections at CMS", *CMS PAS* **JME-07-002** (2008).

[10] T. Sjostrand, S. Mrenna, and P. Skands, "PYTHIA 6.4 physics and manual", *JHEP* **05:026** (2007).

[11] S. Agostinelli et al., "Geant 4 – A Simulation Toolkit", *Nucl. Inst. Meth. A* **506** (2003) 250–303. doi:10.1016/S0168-9002(03)01368-8.

[12] CMS Collaboration, "Offset Energy Correction for Cone Jets", *CMS PAS* **JME-09-003** (2009).

[13] UA2 Collaboration, "Measurement of Production and Properties of Jets at the CERN anti-p p Collider", *Z. Phys.* **C20** (1983) 117. doi:10.1007/BF01573214.

[14] D0 Collaboration, "Determination of the absolute jet energy scale in the D0 calorimeters", *Nucl. Inst. Meth. A* **424** (1999) 352–394. doi:10.1016/S0168-9002(98)01368-0.

[15] CDF Collaboration, "Determination of the jet energy scale at the Collider Detector at Fermilab", *Nucl. Inst. Meth. A* **566** (2006) 375–412. doi:arXiv:hep-ex/0510047.

[16] CMS Collaboration, "Determination of the Relative Jet Energy Scale at CMS from Dijet Balance", *CMS PAS* **JME-08-003** (2009).

[17] CMS Collaboration, "Single Particle response in the CMS Calorimeters", *CMS PAS* **JME-10-008** (2010).

[18] CMS Collaboration, "Jet energy calibration with photon+jet events", *CMS PAS* **JME-09-004** (2009).

[19] D0 Collaboration, "High p_{T} jets in $p\bar{p}$ collisions at $\sqrt{s} = 630\,\mathrm{GeV}$ and $1800\,\mathrm{GeV}$", *Phys.Rev.D64* **032003** (2000).

[20] CMS Collaboration, "Measurement of the Jet Energy Resolutions and Jet Reconstruction Efficiency at CMS", *CMS PAS* **JME-09-007** (2009).

[21] CMS Collaboration, "Measurement of Momentum Scale and Resolution using Low-mass resonances and Cosmic-Ray Muons", *CMS PAS* **TRK-10-004** (2010).

[22] CMS Collaboration, "Electromagnetic calorimeter calibration with 7 TeV data", *CMS PAS* **EGM-10-003** (2010).